

A SYSTEMATIC SURVEY OF PROTOCLUSTERS AT $z \sim 3\text{--}6$ IN THE CFHTLS DEEP FIELDS

JUN TOSHIKAWA¹, NOBUNARI KASHIKAWA^{1,2}, RODERIK OVERZIER³, MATTHEW A. MALKAN⁴, HISANORI FURUSAWA¹, SHOGO ISHIKAWA², MASAFUSA ONOUE², KAZUAKI OTA^{5,6}, MASAYUKI TANAKA¹, YUU NIINO¹, AND HISAKAZU UCHIYAMA²

¹Optical and Infrared Astronomy Division, National Astronomical Observatory, Mitaka, Tokyo 181-8588, Japan; jun.toshikawa@nao.ac.jp

²Department of Astronomy, School of Science, Graduate University for Advanced Studies, Mitaka, Tokyo 181-8588, Japan

³Observatório Nacional, Rua José Cristino, 77. CEP 20921-400, São Cristóvão, Rio de Janeiro-RJ, Brazil

⁴Department of Physics and Astronomy, University of California, Los Angeles, CA 90095-1547, USA

⁵Kavli Institute for Cosmology, University of Cambridge, Madingley Road, Cambridge CB3 0HA, UK

⁶Cavendish Laboratory, University of Cambridge, 19 J. J. Thomson Avenue, Cambridge CB3 0HE, UK

Received 2015 July 8; revised 2016 April 21; accepted 2016 April 27; published 2016 July 26

ABSTRACT

We present the discovery of three protoclusters at $z \sim 3\text{--}4$ with spectroscopic confirmation in the Canada–France–Hawaii Telescope Legacy Survey Deep Fields. In these fields, we investigate the large-scale projected sky distribution of $z \sim 3\text{--}6$ Lyman-break galaxies and identify 21 protocluster candidates from regions that are overdense at more than 4σ overdensity significance. Based on cosmological simulations, it is expected that more than 76% of these candidates will evolve into a galaxy cluster of at least a halo mass of $10^{14} M_{\odot}$ at $z = 0$. We perform follow-up spectroscopy for eight of the candidates using Subaru/FOCAS, Keck II/DEIMOS, and Gemini-N/GMOS. In total we target 462 dropout candidates and obtain 138 spectroscopic redshifts. We confirm three real protoclusters at $z = 3\text{--}4$ with more than five members spectroscopically identified and find one to be an incidental overdense region by mere chance alignment. The other four candidate regions at $z \sim 5\text{--}6$ require more spectroscopic follow-up in order to be conclusive. A $z = 3.67$ protocluster, which has 11 spectroscopically confirmed members, shows a remarkable core-like structure composed of a central small region (<0.5 physical Mpc) and an outskirts region (~ 1.0 physical Mpc). The Ly α equivalent widths of members of the protocluster are significantly smaller than those of field galaxies at the same redshift, while there is no difference in the UV luminosity distributions. These results imply that some environmental effects start operating as early as at $z \sim 4$ along with the growth of the protocluster structure. This study provides an important benchmark for our analysis of protoclusters in the upcoming Subaru/HSC imaging survey and its spectroscopic follow-up with the Subaru/PFS that will detect thousands of protoclusters up to $z \sim 6$.

Key words: early universe – galaxies: clusters: general – galaxies: high-redshift – large-scale structure of universe

1. INTRODUCTION

Galaxy clusters in the early universe provide key clues to the relation between structure formation and galaxy evolution. In the local universe, galaxy clusters are located in the densest peaks of the dark matter distribution at the intersections of filaments (e.g., de Lapparent et al. 1986). Their galaxies have properties significantly different from field galaxies, as evidenced by the morphology–density relation and the cluster red sequence (e.g., Visvanathan & Sandage 1977; Dressler 1980). In this way, cluster formation is closely linked to the large-scale structure and environmental effects on galaxy properties. The direct observation of protoclusters, which are overdense regions of galaxies in the high-redshift universe, will provide us clues to how these relations are formed.

In the local universe, clusters contain a large number of passive galaxies, but the fraction of star-forming galaxies in clusters gradually increases with redshift (e.g., Butcher & Oemler 1984). Around $z \sim 1$, some studies reported that galaxies in high-density environments form stars more actively than those in low-density environments (e.g., Tran et al. 2010; Popesso et al. 2011). Beyond $z \sim 2$, young and star-forming galaxies appear to be a dominant galaxy population even in the most overdense regions. These protoclusters are often identified by using Lyman-break galaxies (LBGs) or Ly α emitters (LAEs), which enable us to trace large-scale structures at high redshift (e.g., Steidel et al. 1998; Venemans et al. 2007; Kuiper et al. 2010; Galametz et al. 2013). The highest-redshift

protocluster discovered to date is at $z = 6.01$ (Toshikawa et al. 2012) and is composed of at least 10 galaxies (Toshikawa et al. 2014). Some candidates without spectroscopic confirmation beyond $z = 6$ have also been found (Trenti et al. 2012; Ishigaki et al. 2016). Although the majority of protocluster members are young and star-forming galaxies, a red sequence, composed of bright and red galaxies, is found to appear in protoclusters around $z \sim 2\text{--}3$ (e.g., Kurk et al. 2004; Kodama et al. 2007; Zirm et al. 2008; Kubo et al. 2013; Lemaux et al. 2014). These color differences between protocluster and field galaxies is the result of different galaxy properties, such as age, dust, or metallicity. For example, stellar mass is a basic and readily observable property that can be used to determine details of the star-formation history (SFH); protocluster galaxies appear to have higher stellar masses than their field counterparts at $z \sim 2\text{--}3$ (Steidel et al. 2005; Kuiper et al. 2010). However, Hatch et al. (2011) reported that the star-formation rate (SFR) is similar between protocluster and field galaxies at $z \sim 2$. These results suggest that the differences in stellar mass at $z \sim 2\text{--}3$ between protocluster and field galaxies may be attributed to differences in star-formation duration or the formation epoch. Besides ordinary galaxies, very rare objects, such as Ly α blobs, submillimeter galaxies (SMGs), and active galactic nuclei (AGNs), are also frequently discovered in high-density environments (Lehmer et al. 2009; Digby-North et al. 2010; Tamura et al. 2010; Matsuda et al. 2011). Some contradictory results in the mass–metallicity relation have been revealed among protoclusters at the same redshift (Kulas et al.

Table 1
Photometric Data and the Number of Dropout Galaxies

Field	R.A. (J2000)	decl. (J2000)	Area (arcmin ²)	u^{*a} (mag)	g'^a (mag)	r'^a (mag)	i'^a (mag)	z'^a (mag)	N_u^b	N_g^b	N_r^b	N_i^b
D1	02:25:59	-04:29:40	3063	28.12	28.32	27.77	27.30	26.39	17110	10416	2433	148
D2	10:00:28	+02:12:30	2902	28.07	28.19	27.70	27.30	26.45	14515	11160	2539	231
D3	14:19:27	+52:40:56	3161	28.14	28.38	27.91	27.48	26.43	21454	14896	2579	232
D4	22:15:31	-17:43:56	3035	27.96	28.19	27.67	27.17	26.26	10484	11288	1926	188

Notes.

^a 3σ limiting magnitude in a $1''.4$ aperture.

^b Number of u -, g -, r -, or i -dropout galaxies.

2013; Kacprzak et al. 2015; Shimakawa et al. 2015; Valentino et al. 2015). Furthermore, Cucciati et al. (2014) have found a large amount of cold gas surrounding a $z = 2.9$ protocluster, which may serve as the reservoir for significant future star formation.

As described above, some distinguishing features have been identified in each protocluster by comparing with field galaxies, but the still relatively small number of protoclusters known (see the overview table in Chiang et al. 2013) makes it difficult to determine which are common features. In addition to the sample size, it should be noted that many previous studies used radio galaxies (RGs) or quasars (QSOs) as probes of protoclusters (e.g., Miley et al. 2004; Venemans et al. 2007; Wylezalek et al. 2013; Adams et al. 2015) because the host galaxies of these objects are thought to be embedded in massive dark matter halos. Hatch et al. (2014) showed that RGs tend to reside in high-density environments; on the other hand, protoclusters are also found in the regions without RGs or QSOs (e.g., Steidel et al. 1998; Ouchi et al. 2005). Despite the efficiency of searching for protoclusters around RG or QSO fields, biased protoclusters might be selected because strong radiation from RGs and QSOs may provide negative feedback and suppress nearby galaxy formation, especially for low-mass galaxies (e.g., Barkana & Loeb 1999; Kashikawa et al. 2007). Furthermore, the mechanisms triggering AGN activity may not be present in all overdense environments and, given that AGN activity is a transient phenomenon with, in some cases, relatively short timescales (e.g., Hopkins 2012), it is likely that many protoclusters are missed when using such objects as beacons. In addition to RGs and QSOs, SMGs have been used as similar probes of overdensities at high redshift (e.g., Capak et al. 2011; Walter et al. 2012; Casey et al. 2015; Smolcic et al. 2016). However, only cursory systematic studies of such objects have been performed (e.g., Aravena et al. 2010), finding that SMGs have a complicated relationship with environment, and, indeed, simulations appear to underscore the complexity of this relationship (Miller et al. 2015). Therefore it is preferable, for any systematic study of such environments, to use a population that minimizes such biases and complexities. This would allow us to address cluster formation and environmental effects on galaxy evolution based on systematic and less-biased samples of protoclusters.

Here, we present a systematic survey of protoclusters at $z \gtrsim 3$ based on wide-field imaging and follow-up spectroscopy. This is a complementary approach to protocluster research compared with previous surveys targeting RG/QSO fields using a relatively small field of view (FoV). This survey was performed using the wide ($\sim 4 \text{ deg}^2$) Canada–France–Hawaii Telescope Legacy Survey (CFHTLS) Deep Fields, whose

depth and area are more adequate for measuring the overdensity of high-redshift galaxies to identify distant protoclusters than the CFHTLS Wide Fields. Although our protocluster candidates were detected by using a less-biased method, our method still relies on the presence of Ly α emission, which will bring another potential bias, in confirming the protocluster members by spectroscopy. Section 2 describes the imaging data and the $z \sim 3$ –6 dropout galaxy sample used in this study. In Section 3, we quantify overdensity based on the sky distribution of $z \sim 3$ –6 galaxies and select the best protocluster candidates by comparing the most overdense regions with expectations from a cosmological simulation. The configuration and results of our follow-up spectroscopy are shown in Section 4. In Section 5, we discuss the structure and properties of confirmed protoclusters and compare with those of field galaxies. The conclusions are given in Section 6. We assume the following cosmological parameters: $\Omega_M = 0.3$, $\Omega_\Lambda = 0.7$, $H_0 = 70 \text{ km s}^{-1} \text{ Mpc}^{-1}$, and magnitudes are given in the AB system.

2. SAMPLE SELECTION

2.1. Photometric Data

We made use of publicly available data from the CFHTLS (T0007: Gwyn 2012), which was obtained with MegaCam mounted at the prime focus of the CFHT. The Deep Fields of the CFHTLS were used in this study, which consist of four independent fields of about 1 deg^2 area each ($\sim 4 \text{ deg}^2$ area in total) observed in the u^* , g' , r' , i' , and z' bands. The field center and limiting magnitudes of each field are summarized in Table 1. The seeing size (FWHM) and pixel scale of all the images are $\sim 0''.7$ and $0''.186$, respectively. Although data at other wavelengths, such as near- or mid-infrared imaging, are available in a part of the CFHTLS Deep Fields, the depth and coverage are significantly different from field to field. Therefore, our protocluster search is conducted only based on the optical data to make a uniform survey.

We created two multicolor catalogs with SExtractor (version 2.8.6; Bertin & Arnouts 1996), in which i' - and z' -band images were used as detection images. The detection images were first smoothed with a Gaussian function; then objects were detected by requiring a minimum of three adjacent pixels each above 1σ of the sky background rms noise. Then, the magnitudes and several other photometric parameters were measured in the other band images at exactly the same positions and with the same aperture of 1.4 arcsec as in the detection-band images using the “double image mode.” The Galactic extinction was removed for each field based on the measurement of Schlafly & Finkbeiner (2011). The individual catalogs were masked to

remove the regions where the detection and photometric measurements of objects may have been seriously affected. These regions are around bright stars and diffraction and bleed spikes from bright stars. The regions near the frame edges, whose depth is systematically shallow, were also excluded. As noted in Gwyn (2012), bright stars with $\lesssim 9$ mag produce a large halo whose radius is ~ 3.5 arcmin. The total masked regions were $\sim 15\%$ – 20% of the FoV, and the effective areas of our analysis are shown in Table 1. Finally, $\sim 330,000$ – $420,000$ and $230,000$ – $270,000$ objects were detected down to the 3σ limiting magnitudes, defined as the magnitude corresponding to three times the standard deviation in the sky flux measured in empty 1.4 arcsec apertures, of the i' and z' bands in each field, respectively. To estimate the detection completeness of each i' - and z' -band image, we used the IRAF task `mkobjects` to create artificial objects on the original images. Artificial objects, which were given a Gaussian profile with a FWHM the same as the seeing size, were randomly distributed on the real image outside of twice the FWHM of the real objects to avoid blending artificial objects with real objects. We generated 50,000 artificial objects in the 20–30 mag range and extracted them using SExtractor with the same parameter set. This procedure was repeated 10 times, and the detection completeness was 70%–50% at the 3σ limiting magnitudes of i' and z' bands in each field. At fainter than 3σ limiting magnitude, the detection completeness drops sharply to $\sim 10\%$. We confirmed that the results of our completeness tests are consistent with the values described in the CFHTLS data release (we find $\sim 84\%$ completeness at the same magnitude at which $\sim 80\%$ is expected). It should be noted that detection completeness at bright magnitudes depends on blending with neighbor objects, and we carefully masked out bright objects.

2.2. Selection of Dropout Galaxies at $z \sim 3$ – 6

We selected $z \sim 3$ – 6 galaxy candidates using the Lyman-break technique (u -, g -, r -, and i -dropout galaxies). The i' -band detection catalog was used for the selection of u -, g -, and r -dropout galaxies, and i -dropout galaxies were selected from the z' -band detection catalog, based on the following color-selection criteria (van der Burg et al. 2010; Toshikawa et al. 2012):

$$\begin{aligned}
 u\text{-dropouts} : & 1.0 < (u^* - g') \wedge -1.0 < (g' - r') \\
 & < 1.2 \wedge 1.5(g' - r') < (u^* - g') - 0.75, \\
 g\text{-dropouts} : & 1.0 < (g' - r') \wedge -1.0 < (r' - i') \\
 & < 1.0 \wedge 1.5(r' - i') < (g' - r') \\
 & - 0.80 \wedge u^* > m_{\text{lim},2\sigma}, \\
 r\text{-dropouts} : & 1.2 < (r' - i') \wedge -1.0 < (i' - z') \\
 & < 0.7 \wedge 1.5(i' - z') < (r' - i') \\
 & - 1.00 \wedge u^*, g' > m_{\text{lim},2\sigma}, \\
 i\text{-dropouts} : & (i' - z') > 1.5 \wedge u^*, g', r' > m_{\text{lim},2\sigma},
 \end{aligned}$$

where $m_{\text{lim},2\sigma}$ is a 2σ limiting magnitude. In redder bands than Lyman break (e.g., g' and r' bands for u -dropout galaxies), we only used objects detected with more than 2σ significance in order to accurately estimate their color; on the other hand, 2σ limiting magnitude was used as the color limit if objects were detected at less than 2σ significance in bluer bands (e.g., u^* band for u -dropout galaxies). The results do not significantly change even if we use 1σ or 3σ significance as the limiting

magnitude. We estimated the redshift distribution resulting from these criteria by using the population synthesis model code GALAXEV (Bruzual & Charlot 2003) and the absorption of the intergalactic medium (IGM) (Madau 1995). In GALAXEV, we simulated a large variety of galaxy spectral energy distributions (SEDs) using the simple stellar population model. We assumed a Salpeter (1955) initial mass function with lower and upper mass cutoffs $m_L = 0.1 M_\odot$ and $m_U = 100 M_\odot$, two metallicities (0.2 and $0.02 Z_\odot$), and two SFHs of constant and instantaneous star formation. We extracted model spectra with ages between 5 Myr and the age of the universe at that redshift and applied the reddening law of Calzetti et al. (2000) with $E(B - V)$ between 0.00 and 1.50. The model magnitudes were estimated by convolving these simulated SEDs with the filter transmission curves. We then added the photometric noise, which is typically $\Delta m = 0.04$ mag and 0.13 mag at the 10σ and 3σ limiting magnitudes, respectively. In this process, we assumed that the magnitude distribution of the simulated galaxies and the observed dropout galaxies were the same. Then, the redshift distributions of the u -, g -, r -, and i -dropout galaxies are estimated by applying the same color-selection criteria of dropout galaxies to these simulated SEDs (Figure 2). The expected redshift ranges of the dropout selections are $z \sim 2.8$ – 3.7 , 3.3 – 4.3 , 4.3 – 5.1 , and 5.7 – 6.5 for u -, g -, r -, and i -dropout galaxies, respectively. It should be pointed out that these estimates rely on some assumptions (e.g., the model of IGM absorption, SFH). Although we used the IGM model of Madau (1995), other models have been proposed (Meiksin 2006; Inoue et al. 2014). Furthermore, Thomas et al. (2014) found that IGM absorption can vary significantly among different lines of sight, but there is a degeneracy between IGM absorption and dust extinction. However, as long as the properties of the galaxies in overdense regions and in the field are not too different, both populations will be affected in the same manner, implying that we can still search for relative overdensities as a tracer of protoclusters. The numbers of selected dropout galaxies detected in each field are shown in Table 1. Note that the limiting magnitude of this study corresponds to about $M_{\text{UV}}^* + 2.6$, $M_{\text{UV}}^* + 2.4$, $M_{\text{UV}}^* + 1.7$, and M_{UV}^* (where M_{UV}^* is the characteristic magnitude of the Schechter functions fitted to the dropout galaxies at each redshift) for u -, g -, r -, and i -dropout galaxies, respectively (Bouwens et al. 2007; van der Burg et al. 2010). Thus, the survey depth reaches at least the typical brightness of dropout galaxies, even for i -dropout galaxies.

We evaluated the contamination rate for these color-selection criteria by comparing the dropout selection regions with the positions of contamination on a two-color diagram (Figure 1). The major sources of the contamination are dwarf stars and old elliptical galaxies, the latter possibly able to satisfy the color criteria due to the 4000 \AA /Balmer break. To estimate the contamination rate of dwarf stars, we use the TRILEGAL code (Girardi et al. 2005), which can simulate number count and broadband photometry of stars in any Galaxy field. Since this model enables us to set up various structural parameters of thin disk, thick disk, halo, and bulge, we used an exponential disk model with default values of scale length and height, and a

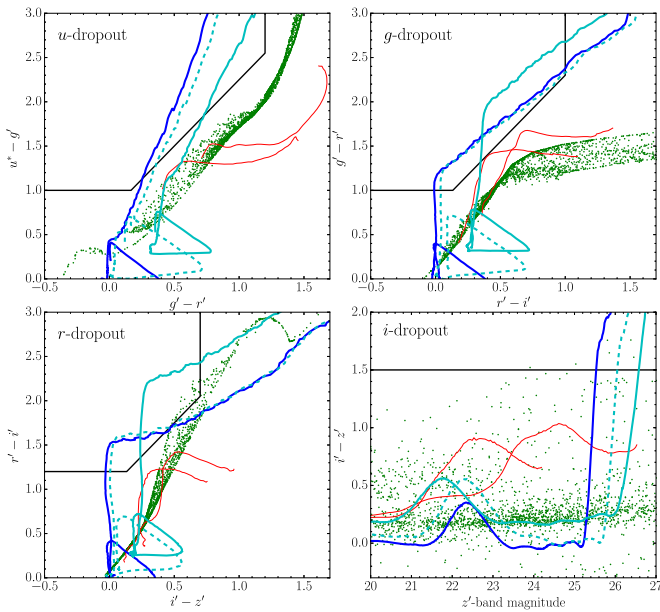


Figure 1. Demonstration of dropout galaxy selection on two-color and color-magnitude diagrams. Thick black lines show the borders of our dropout galaxy selection (see Section 2.2). Blue lines indicate redshift evolution tracks of young star-forming galaxies (age = 100 Myr, $E(B - V) = 0.1$), and cyan lines indicate the same as blue lines but for $E(B - V) = 0.4$ (solid) and age = 600 Myr (dashed). Two red lines are redshift evolution tracks of elliptical galaxies at $z = 0-1.5$ with ages of 1 and 7 Gyr, and green dots are dwarf stars estimated by the TRILEGAL galactic model (Girardi et al. 2005). Note that redshift evolution tracks in the i -dropout panel can shift horizontally depending on the assumption of stellar mass, since the x axis is magnitude, not color.

Chabrier IMF was applied. The galactic latitudes were set to be the same as those of the observations ($|b| = 40 - 60^\circ$). Then, photometry of the simulated dwarf stars was calculated for the filter set for CFHT/MegaCam. Next, we simulated old galaxy SEDs using the GALAXEV, assuming two relatively high metallicities (Z_\odot and $2.5Z_\odot$), and we extracted model spectra with ages of 1.0–10.0 Gyr. The redshift tracks of old galaxies are away from all dropout selection regions. And, although a few dwarf stars are located only within the r - and i -dropout selection regions, the main locus of dwarf stars lies far from these regions. Actually, the contamination rate of dwarf stars in the r -dropout samples is expected to be 2.2%–7.8% depending on the galactic latitude, and the contamination rate in i -dropout samples is 3.4%–6.4% in the CFHTLS Deep Fields. Based on these simulations of dwarf stars and old galaxies, the dropout selection criteria used in this study are confirmed to be able to separate high-redshift galaxies from contaminations.

3. PROTOCLUSTER CANDIDATES

3.1. Sky Distribution and Selection of Significant Overdensities of Dropout Galaxies

We have estimated the local surface number density by counting the number of dropout galaxies within a fixed aperture in order to determine the overdensity significance quantitatively. Chiang et al. (2013) presented a useful definition of the characteristic radius of protoclusters based on cosmological simulations, which encloses 65% of the mass, based on a combination of N -body dark matter simulations and semianalytical galaxy-formation models. Although their result was based on the three-dimensional distribution of protocluster

galaxies, it is still a useful guide for constructing a map of the projected local surface number density when searching for protoclusters. According to the characteristic radius of protoclusters having a descendent halo mass of $1-3 \times 10^{14} M_\odot$ at $z = 0$, the radius of 0.75 physical Mpc was used for u -, g -, and r -dropout galaxies, which correspond to 1.6, 1.8, and 1.9 arcmin, respectively. Although the characteristic radius is expected to be larger for protoclusters having more massive descendent masses, these still show a clear overdensity even on 0.75 physical Mpc scales; thus, the aperture size of 0.75 physical Mpc should be effective to find protoclusters with a descendent halo mass of $>1 \times 10^{14} M_\odot$. However, we still have to consider the projection effects resulting from the large redshift uncertainty of our dropout selection. We discuss the effectiveness of our protocluster search more quantitatively by using a theoretical model in the following subsection. It should be noted that protoclusters have a nearly constant physical size at $z \gtrsim 3$ (Chiang et al. 2013; Muldrew et al. 2015). We used a slightly larger radius of 1.0 physical Mpc (2.9 arcmin) for i -dropout galaxies in order to reduce the large Poisson error resulting from a too-small aperture. The apertures were distributed over the CFHTLS Deep Fields in a grid pattern at intervals of $\sim 20''$. We measured the mean and the dispersion, σ , of the number of galaxies in an aperture over the field. The surface number density in masked regions was assumed to be the same as the mean surface number density. Apertures in which more than 5% area is masked are not used in the following analysis. Using the mean and σ of the number of dropout galaxies in an aperture, surface number density contours of u -, g -, r -, and i -dropout galaxies were calculated and are plotted in Figures 3–6, respectively. We note that this is the same procedure that was applied to the i -dropout galaxies in the Subaru Deep Field (SDF) to draw their surface number density contour, which led to the discovery of the protocluster at $z = 6.01$ from Toshikawa et al. (2012, 2014). In order to study the effects of incompleteness, we performed the same overdensity measurement but for u -, g -, and r -dropout galaxies brighter than 26.0 mag in the i' band (for i -dropout galaxies, it is hard to select a brighter subset because of the small sample size). From this analysis, we confirmed that the change of limiting magnitude does not have a significant effect on our protocluster selection.

3.2. Comparison with Cosmological Simulations

Although we can clearly see some overdense regions in the sky distribution maps presented in Figures 3–6, it is not straightforward to find plausible protocluster candidates since the large redshift uncertainty of the dropout technique, which is $\Delta z \sim 1$ ($\sim 230 - 60$ physical Mpc at $z \sim 3.1-6.0$), hampers the identification of clustering structure in three-dimensional space. On one hand, overdensities associated with real protoclusters could be weakened by fore- or background galaxies; on the other hand, chance alignments of the large-scale structure or superpositions of filaments could erroneously enhance the surface overdensity. Therefore, we will make use of predictions from simulations to understand the relation between surface overdensity significance and the probability of finding real protoclusters.

To this end, we used a set of light-cone models constructed by Henriques et al. (2012). A brief outline of the light-cone models is presented below. First, the assembly history of the dark matter halos was traced using an N -body simulation

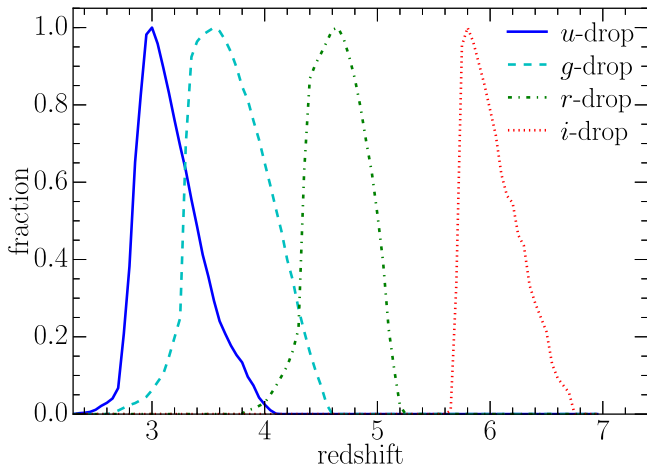


Figure 2. Expected redshift distribution of u -, g -, r -, and i -dropout galaxies.

(Springel et al. 2005), in which the length of the simulation box was $500 h^{-1} \text{Mpc}$ and the particle mass was $8.6 \times 10^8 h^{-1} M_{\odot}$. The distributions of dark matter halos were stored at discrete epochs. Next, the processes of baryonic physics were added to dark matter halos at each epoch using a semianalytic galaxy-formation model (Guo et al. 2011). Based on the intrinsic parameters of galaxies predicted by the semianalytic model, such as stellar mass, SFH, metallicity, and dust content, the photometric properties of simulated galaxies were estimated from the stellar population synthesis models developed by Bruzual & Charlot (2003). Then, these simulated galaxies in boxes at different epochs were projected along the line of sight, and intergalactic medium (IGM) absorption was applied (Madau 1995) in order to mimic a pencil-beam survey, as described in Overzier et al. (2013). Finally, 24 light-cone models with $1.4 \times 1.4 \text{ deg}^2$ FoV were extracted using these procedures.

The simulated u -, g -, r -, and i -dropout galaxy catalogs were made by matching the expected redshift distribution of each dropout galaxy sample (Figure 2).⁷ We also applied the same limiting magnitude cut only for the detection band used for the observations to the simulated catalogs (i band for u -, g -, r -dropout galaxies, and z band for i -dropout galaxies). The average stellar mass of these simulated dropout galaxies is $\sim 2 \times 10^9 M_{\odot}$, and the 90% quantile range is $\sim 2 \times 10^8$ to $1 \times 10^{10} M_{\odot}$. This is consistent with that observed (e.g., Stark et al. 2009), implying that simulated dropout galaxies trace similar structures. Based on these simulated catalogs, we calculated local number density maps as in Section 3.1 and selected overdense regions in the same way as in the CFHTLS Deep Fields. For each overdense region of dropout galaxies, we selected the strongest spike in the redshift distribution, and the dominant dark matter structure was defined by the most massive halo in that redshift spike. The descendent halos at $z = 0$ for each overdense region were then easily identified by tracing the halo merger tree of those halos. As shown in Figure 7, although there is a large scatter, the significance of the

⁷ Ideally, we should select the dropout galaxies from the simulations by applying the same color-selection criteria to the simulated catalogs. However, because some systematic differences exist between the simulated and real galaxies in color-color space, this method will be explored in the future as the quality of the simulated catalogs improves.

overdensity at high redshift is clearly correlated with the descendent halo mass at $z = 0$, whose probability of no correlation is < 0.01 based on the Spearman rank correlation test. Thus, it is possible to select reliable protocluster candidates through the surface overdensity. In this study, we set the criterion of protocluster candidates at $> 4\sigma$ overdensity significance in order to obtain a high purity of real protoclusters. Based on this criterion, 76 (90)% of these candidates of u -dropout (i -dropout) galaxies are expected to be in real protoclusters. However, the completeness is very small ($\sim 5\%$ and 10% for u - and i -dropout galaxies), mainly due to the projection effect of the dropout technique. It should be noted that the average descendent mass of protoclusters with $> 4\sigma$ overdensity significance is $\sim 5 \times 10^{14} M_{\odot}$ (Figure 7). A total of 21 candidates were identified from $z \sim 3$ to $z \sim 6$ (five, five, six, and five candidates for the maps of u -, g -, r -, and i -dropout galaxies, respectively). The coordinates and overdensity of the protocluster candidates are listed in Table 2. Since these numbers of protocluster candidates are consistent with the model prediction, in which ~ 2.9 – 6.4 candidates per observed area ($\sim 4 \text{ deg}^2$) are found in each redshift bin from $z \sim 3$ to $z \sim 6$, most of the candidates are expected to be real protoclusters. To summarize, from the wide-field imaging of the CFHTLS Deep Fields, we have made a large protocluster sample at $z \sim 3$ – 6 without the aid of any special probes, such as QSOs, RGs, or SMGs; thus, this sample is not only large but also complementary with previous studies targeting QSO, RG, or SMG fields.

4. FOLLOW-UP SPECTROSCOPY

Despite our calibration of the selection of the protocluster candidates using light-cone projections described in the previous section, the overdense regions discovered could still be attributed to mere chance alignments along the line of sight, given that the dropout technique samples a broad range of redshifts. Another possibility is that the overdense significance could be affected by the presence of highly clustered contaminating populations. This possibility is negligible for the u -, g -, and r -dropout samples because of their high number density. However, for the i -dropout galaxies, the average number density per aperture is only 1.6, due to the shallow z' -band depth. Since the contamination rate of i -dropout galaxies is $\sim 5\%$ (Section 2.2), the number of contaminants in an aperture is $0.0_{-0.0}^{+1.8}$ on average, which could result in an overdensity $\sim 2\sigma$ higher at worst. Therefore, further confirmation of clustering in redshift space is required to see whether our candidates are real or not. In addition to protocluster confirmation, spectroscopic observations enable us to inquire into the internal structure or line properties of protoclusters. It is necessary for revealing cluster formation to take various viewpoints.

Before performing the follow-up spectroscopic observations, we first investigated how far protocluster members are typically spread from the center, again using the light-cone model. In the model, protocluster members are defined as galaxies whose descendants at $z = 0$ reside in $> 10^{14} M_{\odot}$ halos (Overzier et al. 2009a; Chiang et al. 2013). The center of a protocluster in three-dimensional space was estimated by using the median R.A., decl., and redshift of all protocluster members. The positional difference between the protocluster center defined above and the peak of the surface overdensity observed is typically less than 0.5 arcmin and is less than 2 arcmin at worst.

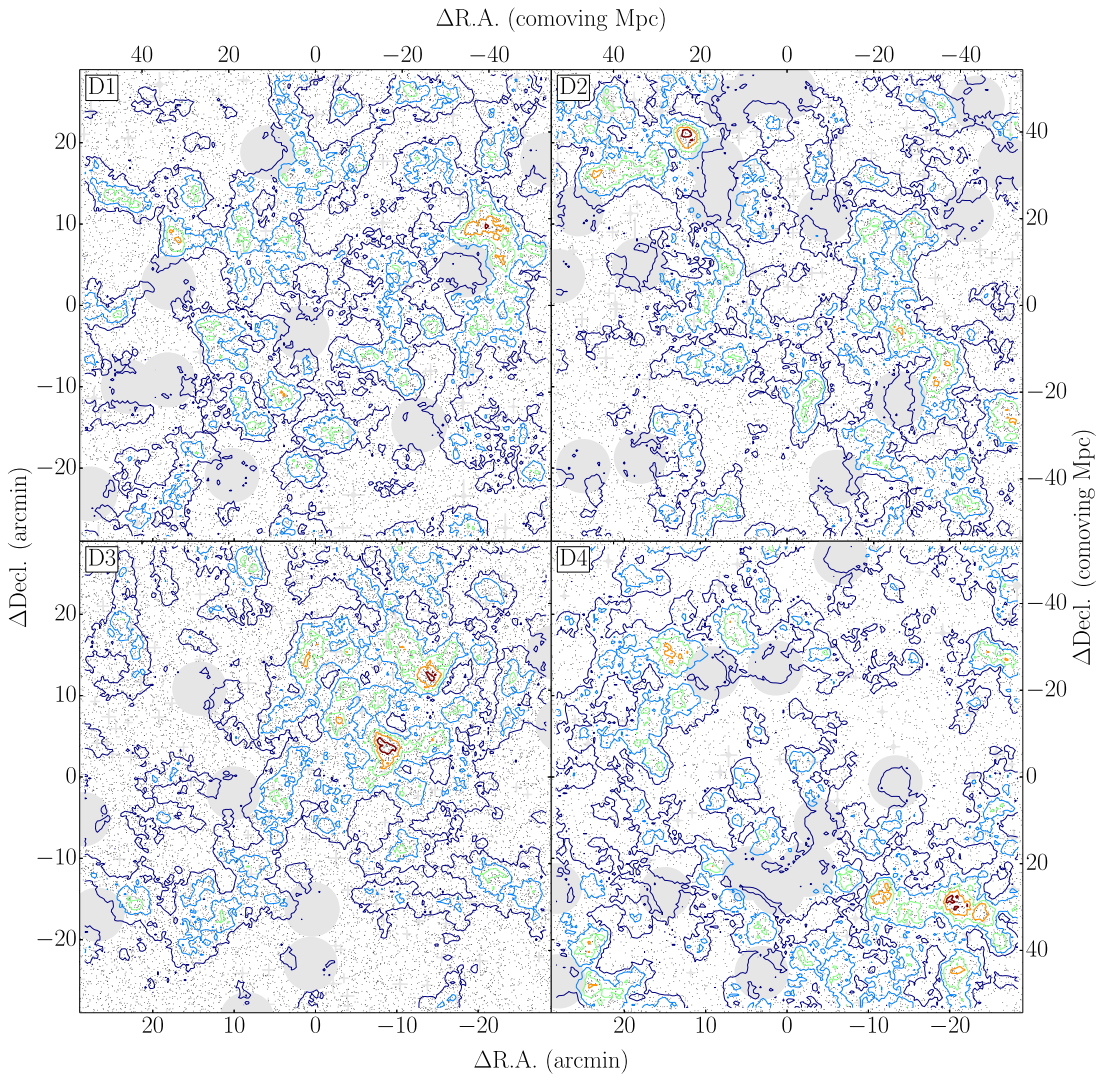


Figure 3. Sky distribution of u -dropout galaxies (dots) with surface number density contours (lines) in the D1 (upper left), D2 (upper right), D3 (lower left), and D4 (lower right) field. The lines correspond to contours of surface overdense significance from 4σ to 0σ (mean) with a step of 1σ . North is up, and east is to the left. The comoving scale projected to $z = 3.1$ is shown along the axes, and masked regions are also shown by gray regions.

Then, we investigated the three-dimensional distribution of protocluster members in the overdense regions. Although each protocluster has a different structural morphology, such as filamentary or sheet-like, we simply estimated the probability of protocluster membership as a function of the distance to the center by calculating the ratio between protocluster members and nonmembers at a certain distance from the center. We finally derive a probability map by taking the median stack of the probability maps of all the protocluster regions computed for each redshift. Figure 8 shows the probability map of protocluster members of u -, g -, r -, and i -dropout galaxies. We found that galaxies lying within the volume of $R_{\text{sky}} < 4(6)$ arcmin and $R_z < 0.010(0.025)$ at $z \sim 3(6)$ will be protocluster members with a probability of $>80\%$. Based on this estimate, we defined the protocluster region as a sphere of 2 physical Mpc radius. It should be noted that we will evaluate protocluster existence based on the significance of excess from a homogeneous distribution rather than the absolute number of confirmed galaxies, because actual observations are incomplete and rely on Ly α emission to identify the redshifts of dropout galaxies. The fraction of Ly α -emitting galaxies among dropout

galaxies has been investigated (e.g., Stark et al. 2011; Curtis-Lake et al. 2012); however, it has yet to be explored for the fraction in overdense regions because the previous studies are mainly based on field galaxies. Overzier et al. (2008) found that a protocluster around a radio galaxy at $z = 4.1$ exhibits a high overdensity of both LAEs and LBGs, while Kashikawa et al. (2007) reported that there is no correlation between the distributions of LAEs and LBGs around a QSO at $z = 4.9$. Hence, it is not yet fully understood what fraction of LBGs emits Ly α , especially in overdense regions. Although this may potentially bias protocluster identification, most protoclusters at $z \sim 2-3$ tend to have high overdensities of both LBGs and LAEs (e.g., Kuiper et al. 2010).

4.1. Observations

We carried out spectroscopic observations using Subaru/FOCAS (Kashikawa et al. 2002), Keck II/DEIMOS (Faber et al. 2003), and Gemini-N/GMOS (Hook et al. 2004). In these observations, eight protocluster candidates from $z \sim 3$ to $z \sim 6$ were observed in total (two at each redshift). The target protocluster candidates and the configuration of spectroscopic

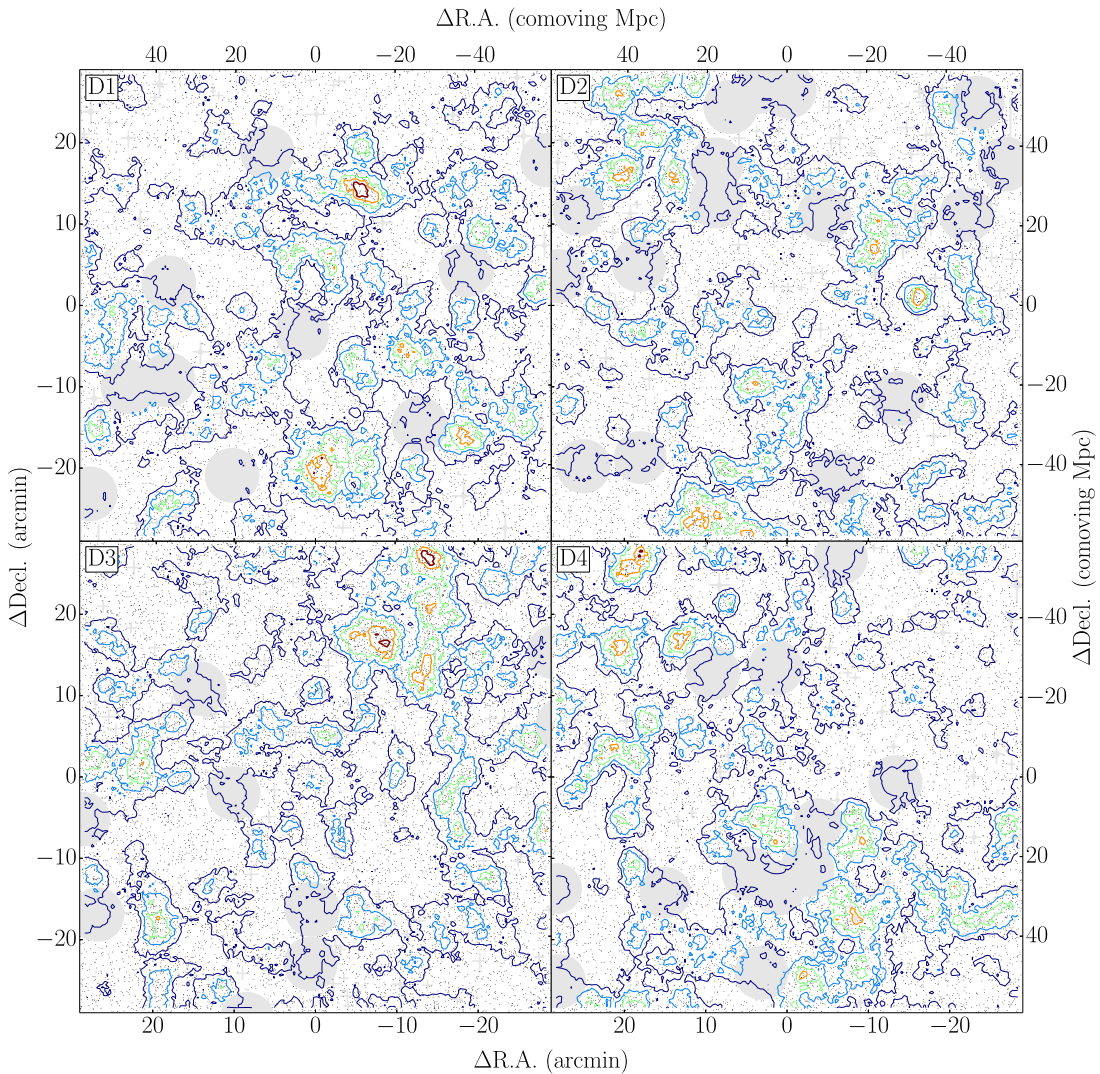


Figure 4. Same as Figure 3, but for the g -dropout galaxies. The comoving scale projected to $z = 3.8$ is shown along the axes.

observations are described in Tables 2 and 3, respectively. All these observations were conducted with Multi-Object Spectroscopy (MOS) mode. The slits typically had a length of 6–8 arcsec and a width of 0.8–1.0 arcsec. The grisms used were selected in order to have the highest efficiency at the wavelength of the redshifted Ly α line of targeted dropout galaxies and the spectral resolution of $<2.8(1 + z_{[\text{O II}]})\text{\AA}$, where 2.8\AA is the wavelength separation of the [O II] doublet ($\lambda = 3726.0, 3728.8\text{\AA}$) in the rest frame. Therefore, our spectroscopic observations were set up to have a resolution that is sufficient to resolve the [O II] emission into the doublet to check for contamination by foreground interlopers. The wavelength coverage is also wide enough to cover the expected redshift range of the dropout galaxies. In the FOCAS observations, the telescope was dithered along the slit to enable more accurate sky subtraction between exposures, and we used nod-and-shuffle mode, which allows an increase in the accuracy of sky subtraction by real-time flipping to the sky position in the GMOS observation. Although higher priority was given to brighter galaxies, we designed slit masks so as to allocate as many objects as possible. Furthermore, a slit of each mask was allocated for a bright star (~ 20 mag) to monitor the

time variations of seeing size or atmospheric transmission between exposures. Although the sky condition was good and stable during all observing nights, we removed only a few poor-quality frames by checking the bright star. Long slit exposures of one of the spectroscopic standard stars HZ44, BD +28d4211, and G191-B2B were taken each night with all configurations used in the night, and we corrected the difference of air mass between science targets and standard stars in the flux calibration. The data taken by FOCAS and GMOS were reduced in a standard manner with IRAF, and the pipeline spec2d⁸ was used for the reduction of the data taken by DEIMOS. The 3σ detection limits of the emission lines are typically 5.0×10^{-18} , 4.0×10^{-18} , 1.0×10^{-18} , and 1.3×10^{-18} erg s $^{-1}$ cm $^{-2}$ for u -, g -, r -, and i -dropout galaxies, respectively, assuming the line width of FWHM = 5.0\AA .

⁸ The data-reduction pipeline was developed at the University of California, Berkeley, with support from National Science Foundation grant AST 00-71048.

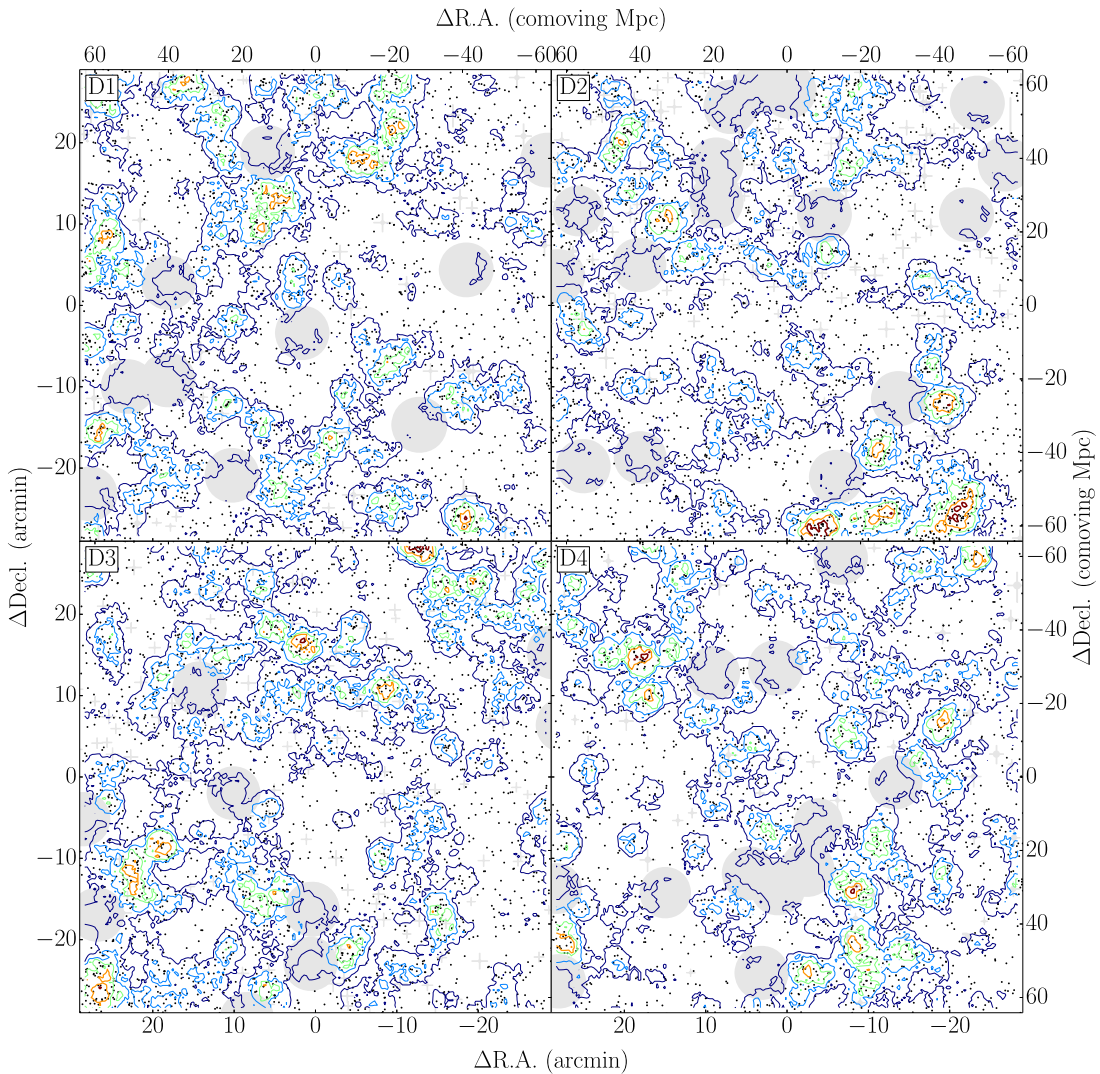


Figure 5. Same as Figure 3, but for the r -dropout galaxies. The comoving scale projected to $z = 4.7$ is shown along the axes.

4.2. Line Contaminations

All emission lines we detected are single emission lines, which are not likely to be $H\beta$ or $[O\text{ III}]\lambda 5007$ emission lines because the wavelength coverage of our observation is wide enough to detect all these multiple lines simultaneously. Only $[O\text{ III}]\lambda 5007$ emission, which is generally the strongest emission among them, might resemble a single emission line if the other lines are too faint to be detected. However, according to the typical line flux ratio of $[O\text{ III}]\lambda 5007$ and $[O\text{ III}]\lambda 4959$ ($f_{\lambda 5007} \sim 3 \times f_{\lambda 4959}$), even $[O\text{ III}]\lambda 4959$ should be detected in our spectroscopic observations since the signal-to-noise ratio (S/N) of detected emission lines is ~ 10 on average (and always > 3). Therefore, we investigated the possibility that $H\alpha$ and $[O\text{ II}]$ emission lines contaminate dropout galaxy samples based on both imaging and spectroscopic data.

Only r - and i -dropout galaxies can be contaminated by $H\alpha$ -emitting galaxies according to its wavelength ($\lambda_{H\alpha} = 6562.8 \text{ \AA}$). Since higher-redshift dropout galaxies are selected using a redder color criterion to detect the strong Lyman break, it is almost impossible to mimic this color by a Balmer break object at lower redshift based on the expected color of passive galaxies, as described in Section 2.2. Even if Balmer breaks of passive and

old galaxies were strong enough to satisfy the dropout color criteria, these stellar populations are unlikely to have $H\alpha$ emission, as a diagnostic of the star-formation activity. On the other hand, dusty starburst galaxies with strong Balmer breaks could be contaminated because they would show a $H\alpha$ emission line as well as a very red color, resulting from the combination of Balmer breaks and dust reddening. However, their $H\alpha$ emissions can be discriminated from $\text{Ly}\alpha$ emissions, which appear right at the Lyman break. Therefore, we consider the possibility of finding foreground $H\alpha$ emission negligible.

Regarding $[O\text{ II}]$ doublet emission lines, it is possible to distinguish between $\text{Ly}\alpha$ and $[O\text{ II}]$ emission lines based on the line profile. The spectral resolution of most of our spectroscopic observations was set high enough to resolve $[O\text{ II}]$ emission lines as doublets ($\Delta\lambda = 3.8\text{--}6.3 \text{ \AA}$ at $z \sim 0.3\text{--}1.3$), although it would be practically difficult to resolve these in most cases because of low S/N. In this case, the $[O\text{ II}]$ emission line is typically skewed blueward, while the $\text{Ly}\alpha$ emission line from high-redshift galaxies is skewed redward. Therefore, the skewness of the line profile allows us to distinguish between $\text{Ly}\alpha$ and $[O\text{ II}]$ emission lines; however, it should be noted that $[O\text{ II}]$ emission is sometimes skewed redward when assuming any exotic physical properties of the $H\text{ II}$ region (e.g., election

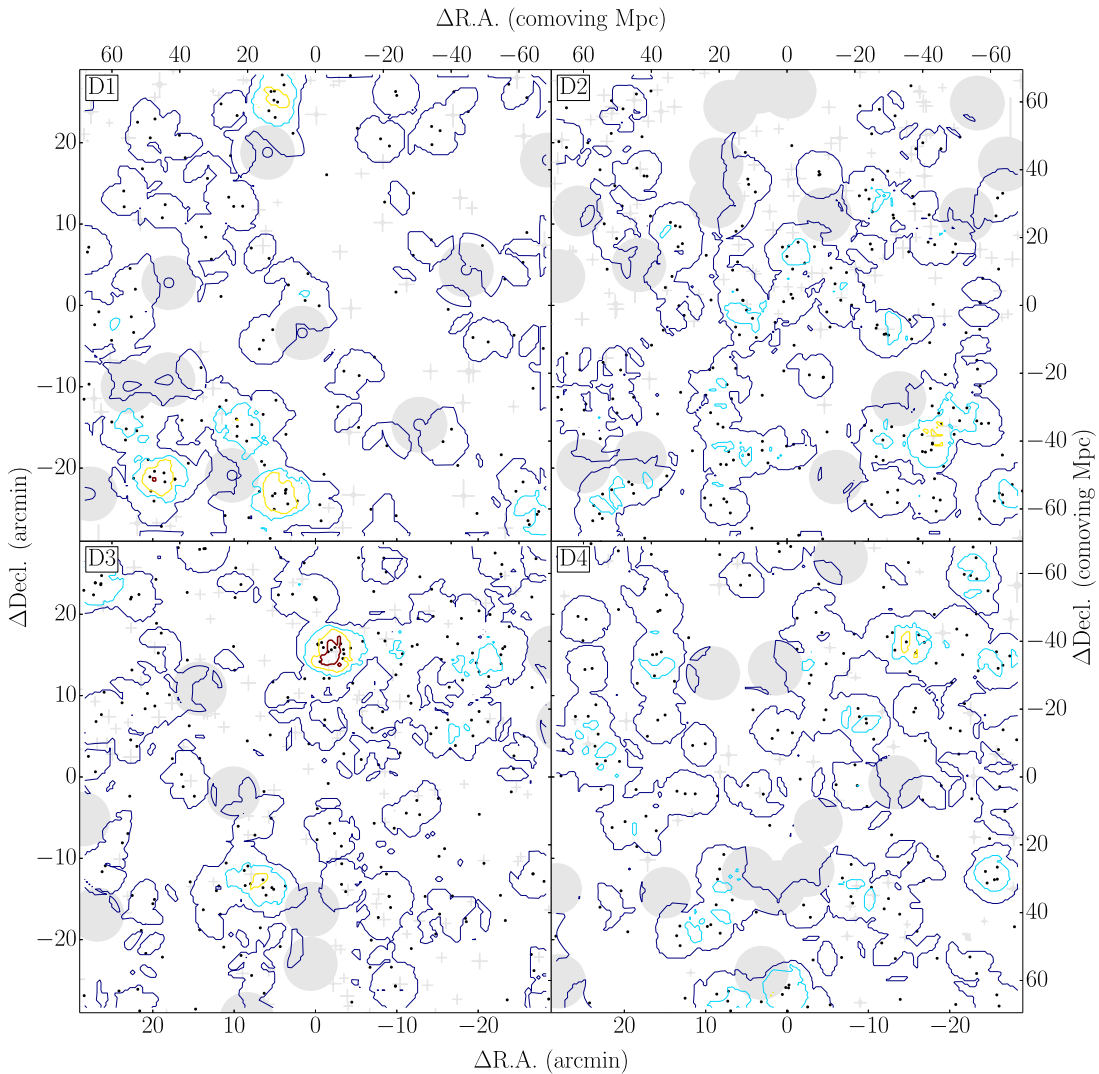


Figure 6. Same as Figure 3, but for the *i*-dropout galaxies, and the lines show overdensity significance from 6σ to 0σ (mean) with a step of 2σ . The comoving scale projected to $z = 5.9$ is shown along the axes.

density). To improve the way they are distinguished, Kashikawa et al. (2006) introduced “weighted” skewness, which makes use of line width as well as line profile. $\text{Ly}\alpha$ emission usually has a larger line width than $[\text{O II}]$ emission because $\text{Ly}\alpha$ emission typically emerges in an outflow or galactic wind. Therefore, we calculated the weighted skewness of all spectroscopically detected galaxies. The asymmetric emission lines with $S_w > 3$ are clear evidence of $\text{Ly}\alpha$ emission from high-redshift galaxies, though it would be more difficult to distinguish them from nearby emission-line galaxies at $z \sim 3$, where the IGM attenuation is weaker than at higher redshifts. As shown in Table 4, most of the emission lines of this study have large S_w . However, 17% of all identified emission lines have $S_w < 3$; although this would be caused by strong sky line residuals and low S/N data, we could not rule out the possibility of $[\text{O II}]$ emission lines. In order to make the line profile measurement more accurate by reducing the effect of sky noise and low S/N data, we made a composite spectrum of all 24 emission lines with $S_w < 3$ by taking a median in the rest frame, assuming they were $\text{Ly}\alpha$, normalized by the peak flux. The weighted skewness of the composite spectrum was found to be $S_w = 8.1 \pm 1.2$, indicating that most of the emission lines

even with $S_w < 3$ in individual spectra are real $\text{Ly}\alpha$ emission lines from high-redshift galaxies. In addition to the line profile, the possibility of $[\text{O II}]$ emission can further be reduced by taking into account photometric data. Although $[\text{O II}]$ emission is closer to Balmer break than $\text{H}\alpha$ emission, it will still be difficult to find a sharp break near the emission line, except for peculiar galaxies such as dusty starburst galaxies.

From these considerations, it is unlikely that $\text{H}\alpha$ or $[\text{O II}]$ emission lines contaminate our dropout samples, and $\text{Ly}\alpha$ is the most plausible interpretation to explain both photometric and spectral features. Since the major contamination in the photometric selection is completely different from that in the spectroscopic observation, the combination of photometric and spectroscopic observations enables us to select a clean sample of high-redshift galaxies. We can regard all single emission lines detected from our dropout sample as $\text{Ly}\alpha$ emission lines.

4.3. Results

Our protocluster confirmation completely depends on the detection of $\text{Ly}\alpha$ emission; therefore, we might only select a part of the galaxy populations in these protoclusters. We might miss protoclusters, if they were mainly composed of passive or

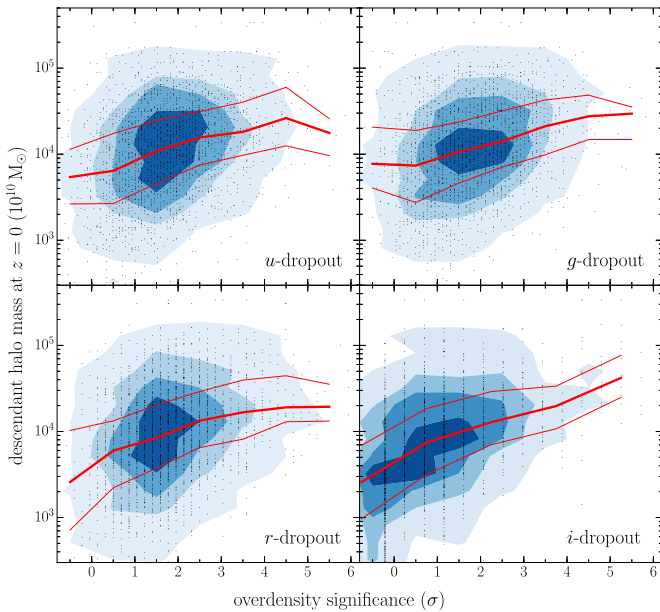


Figure 7. Relation between surface overdensity of u -, g -, r -, and i -dropout galaxies and descendant halo mass at $z = 0$. The thick and thin red lines are the median, upper, and lower quartiles. The background contours show the 25%, 50%, 75%, and 95% regions from dark to light.

dusty galaxies without Ly α emission. This may lead to a possible selection bias in our protocluster search. However, protoclusters at $z \sim 2$ – 3 have been found to mainly contain star-forming galaxies. It is worth noting that known protoclusters that include a large number of older or dustier galaxies, like the SSA22 ($z = 3.1$) and the spiderweb ($z = 2.2$) protoclusters, also show a significant overdensity in LAEs (Steidel et al. 2000; Kuiper et al. 2010; Kubo et al. 2013). These results suggest that the possible bias introduced by tracing protoclusters only by LAEs is probably not significant.

The number of dropout galaxies located in each protocluster candidate region is listed in Table 2, and the number of spectroscopically observed galaxies is shown in Table 5. From these numbers, about half, or at least 35%, of dropout galaxies in protocluster candidate regions were observed by our follow-up spectroscopic observations. We carefully discriminated real emission lines from sky lines or noise by examining both two-dimensional and one-dimensional spectra, and all emission lines identified in this study are shown in Figure 9. We estimate the observed properties of the spectroscopically confirmed galaxies, such as UV absolute magnitude at 1300 Å in the rest frame (M_{UV}), Ly α luminosity ($L_{Ly\alpha}$), and rest-frame Ly α equivalent width (EW_0), shown in Table 4. The redshifts were derived by the peak wavelength of the Ly α emission line, assuming the rest wavelength of Ly α to be 1215.6 Å. These measurements could be overestimated if there was a galactic outflow. When emission lines are located near strong sky lines, the position of the peak could be shifted. These effects of sky lines and the wavelength resolution are taken into account when estimating the error. Observed line flux, $f_{Ly\alpha}$, corresponds to the total amount of the flux within the line profile. The slit loss was corrected based on the ratio of slit width and seeing size for each observation, and its flux error was estimated from the combination of the line width and the noise level per 1 Å at wavelengths blueward of Ly α . Since continuum flux was too faint to be detected in the observed

spectra, M_{UV} was estimated from the broadband magnitude (g' , r' , i' , and z' bands for u -, g -, r -, and i -dropout galaxies). The M_{UV} is defined as the absolute magnitude at 1300 Å in the rest-frame. It is derived from the broadband photometry after correcting the contribution of IGM absorption and the Ly α emission to the broadband photometry based on the spectroscopic. In this calculation, we have assumed a UV slope β ($f_\lambda \propto \lambda^\beta$) to be -2 , which is consistent with the previous observations (e.g., Bouwens et al. 2012). The broadband magnitude has a negligible dependence on UV slope because the broadband width is only ~ 1000 – 1500 Å. We have confirmed that M_{UV} changes only a few percent at maximum when the UV slope was varied from -3.0 to -1.0 . In addition, EW_0 was estimated by combining $f_{Ly\alpha}$ and M_{UV} . The results found for each region are described in the following subsections.

4.3.1. The i -Dropout Protocluster Candidate in the D1 Field

We have observed eight i -dropout galaxies in the D1ID01 region out of 10 candidates. Almost all i -dropout galaxies in the D1ID01 region were spectroscopically observed, as shown in Figure 10. Three galaxies clearly have single emission lines, which can be identified as Ly α emission lines of $z \sim 6$ galaxies. Their photometric and spectroscopic properties are summarized in Table 4. Two of three galaxies (ID = 1 and 2) have close redshifts with a difference of $\Delta z = 0.08$, corresponding to the radial distance of 4.7 Mpc in the physical scale. From our selection criteria, we can expect an ~ 0.2 – 0.4 galaxy in a $\Delta z = 0.1$ bin if they were homogeneously distributed in redshift space. The possibility to have two galaxies within $\Delta z < 0.1$ is 16%. Although their distribution is more concentrated than homogeneous, these two galaxies are unlikely to merge into a single halo by $z = 0$ based on our analysis of the possible separations of protocluster galaxies at $z \sim 6$ (Figure 8). For now, we cannot conclude that there is a real protocluster in the D1ID01 region because of the small number of statistics.

4.3.2. The i -Dropout Protocluster Candidate in the D3 Field

As for the D3ID01 region, eight i -dropout galaxies were observed out of 16 candidates. The completeness of our spectroscopic observation is smaller ($\sim 50\%$) than for the D1ID01 region, which has fewer protocluster member candidates. Many faint i -dropout galaxies are still to be observed because we assigned higher priorities to the brighter i -dropout galaxies. Ly α emission lines were detected from two of the eight spectroscopic targets. The sky distribution of the targets is shown in Figure 11. Table 4 describes the properties of the spectroscopically confirmed galaxies. These two galaxies have almost the same redshift with a difference of $\Delta z < 0.01$ (< 0.5 Mpc in physical scale). The possibility that two galaxies have this small redshift separation is only 1.2%, and these two galaxies can certainly be expected to be in the same halo at $z = 0$ based on this small separation. While we could not make a clear conclusion because of the small number of confirmed galaxies, the discovery of a close galaxy pair at $z \sim 6$ could imply the existence of a protocluster. Interestingly, Toshikawa et al. (2014) have found that galaxies tend to be in close pairs in another protocluster at $z = 6.01$.

The relatively small number of confirmed candidates can be attributed to the observational limit since our spectroscopic

Table 2
Overview of the Protocluster Candidates

Name	R.A. (J2000)	decl. (J2000)	Field	Population	Overdensity ^a	N_{galaxy} ^b	Spec. ^c
D1UD01	02:24:35.4	-04:19:58.9	D1	<i>u</i> -dropout	4.2σ	244	Yes
D2UD01	10:01:18.6	+02:33:20.3	D2	<i>u</i> -dropout	4.6σ	182	No
D3UD01	14:18:29.1	+52:44:05.3	D3	<i>u</i> -dropout	4.8σ	300	No
D3UD02	14:17:52.0	+52:53:03.2	D3	<i>u</i> -dropout	4.4σ	268	No
D4UD01	22:14:03.4	-17:58:43.4	D4	<i>u</i> -dropout	4.4σ	157	Yes
D1GD01	02:25:36.3	-04:15:57.4	D1	<i>g</i> -dropout	5.5σ	162	Yes
D1GD02	02:25:56.2	-04:48:30.4	D1	<i>g</i> -dropout	4.2σ	153	No
D3GD01	14:18:28.9	+52:57:06.5	D3	<i>g</i> -dropout	4.7σ	214	No
D3GD02	14:17:55.6	+53:07:37.6	D3	<i>g</i> -dropout	4.5σ	201	No
D4GD01	22:16:47.3	-17:16:52.7	D4	<i>g</i> -dropout	4.3σ	153	Yes
D1RD01	02:24:45.3	-04:55:56.5	D1	<i>r</i> -dropout	4.4σ	40	Yes
D2RD01	10:00:14.1	+01:44:03.0	D2	<i>r</i> -dropout	4.9σ	48	No
D2RD02	09:59:04.6	+01:47:27.5	D2	<i>r</i> -dropout	4.5σ	64	No
D3RD01	14:19:36.8	+52:57:44.6	D3	<i>r</i> -dropout	4.5σ	39	No
D4RD01	22:14:58.1	-17:58:07.2	D4	<i>r</i> -dropout	4.2σ	31	No
D4RD02	22:16:46.1	-17:29:16.7	D4	<i>r</i> -dropout	4.1σ	31	Yes
D1ID01	02:27:18.4	-04:50:58.9	D1	<i>i</i> -dropout	6.1σ	10	Yes
D1ID02	02:26:19.9	-04:51:55.0	D1	<i>i</i> -dropout	5.5σ	9	No
D3ID01	14:19:14.2	+52:55:15.7	D3	<i>i</i> -dropout	7.6σ	16	Yes
D3ID02	14:20:09.3	+52:28:17.1	D3	<i>i</i> -dropout	4.7σ	10	No
D4ID01	22:14:29.6	-17:27:25.4	D4	<i>i</i> -dropout	4.1σ	7	No

Notes.

^a Overdensity at the peak.

^b Number of dropout galaxies within 3 arcmin radius from its overdensity peak.

^c The protocluster candidates observed by follow-up spectroscopy are marked as “Yes.”

samples are biased to brighter galaxies ($M_{\text{UV}} < -20.75$). We compared the D3ID01 protocluster candidate with the $z = 6.01$ protocluster in the SDF (Toshikawa et al. 2014), which was also identified by the combination of dropout selection and follow-up spectroscopy targeting Ly α emission like this study. Applying the same magnitude limit of $M_{\text{UV}} < -20.75$ to the SDF protocluster, the number of remaining protocluster members was only two out of a total of 10. Furthermore, Ouchi et al. (2005) reported the discovery of two protoclusters at $z \sim 5.7$. These were discovered from a narrow-band survey, and six and four LAEs are included in each protocluster. Although LAE selection is different from our dropout selection, it is useful to check the distribution of the UV continuum and the Ly α luminosity of protocluster galaxies. Based on our observational limits of UV continuum and Ly α luminosity, only about two LAEs would be identified for these protoclusters. Therefore, it is not unreasonable to expect only two confirmed member galaxies in this study even if there is a real protocluster.

4.3.3. The *r*-Dropout Protocluster Candidate in the D1 Field

We have spectroscopically observed 15 *r*-dropout galaxies in the D1RD01 region, and we detected single emission lines from six galaxies. The sky distribution of the observed galaxies is shown in Figure 12. In the $>1\sigma$ overdense region, there are ~ 40 galaxies; thus, only $\sim 38\%$ *r*-dropout galaxies were observed by the follow-up spectroscopy. Two galaxies (ID = 5 and 6) out of six are clustering both in spatial ($\Delta_{\text{sky}} = 33$ arcsec) and redshift space ($\Delta z = 0.004$) at $z = 4.89$ and whose three-dimensional separation is 0.7 Mpc in the physical scale. Considering the observed volume (3 arcmin radius and $\Delta z \sim 0.8$), it is unlikely ($<1\%$) that the close pair is reproduced by a uniform random distribution of six galaxies in

three-dimensional space. However, it is unclear whether this galaxy pair will grow into a cluster at $z = 0$ because of the small number of confirmed galaxies; at least, these two galaxies are expected to merge into a single halo. Since there are many spectroscopically unobserved galaxies, further follow-up observations will enable us to clarify whether there is a protocluster or not.

4.3.4. The *r*-Dropout Protocluster Candidate in the D4 Field

In the D4RD02 region, the total integration time of follow-up spectroscopic observation was only 2 hr, which was half of that in the D1RD01 region. Thus, although 12 *r*-dropout galaxies were observed, Ly α emission lines were detected from only three galaxies. The sky distribution of the observed galaxies is shown in Figure 13. These three galaxies are largely separated in redshift space. Since about 20 *r*-dropout galaxies remain to be spectroscopically observed, further follow-up observations will be necessary to draw a conclusion.

4.3.5. The *g*-Dropout Protocluster Candidate in the D1 Field

Combining the DEIMOS and FOCAS follow-up observations, 123 *g*-dropout galaxies were observed, and the redshifts of 36 galaxies were determined by detecting Ly α emission lines. The sky distribution of the observed galaxies is shown in Figure 14. Figure 15 shows the redshift distribution of confirmed galaxies. Although galaxies seem to be clustering at $z \sim 3.8$, these galaxies are spread over a large projected area, as shown in Figure 14. Since the DEIMOS has a wide FoV ($\sim 16.7 \times 5.0$ arcmin²), which is larger than the area of the D1GD01 region, some *g*-dropout galaxies outside the overdense region were also observed. When we focus only on galaxies in the overdense region, shown by the red-line histogram in Figure 15, the peak around $z = 3.8$ becomes

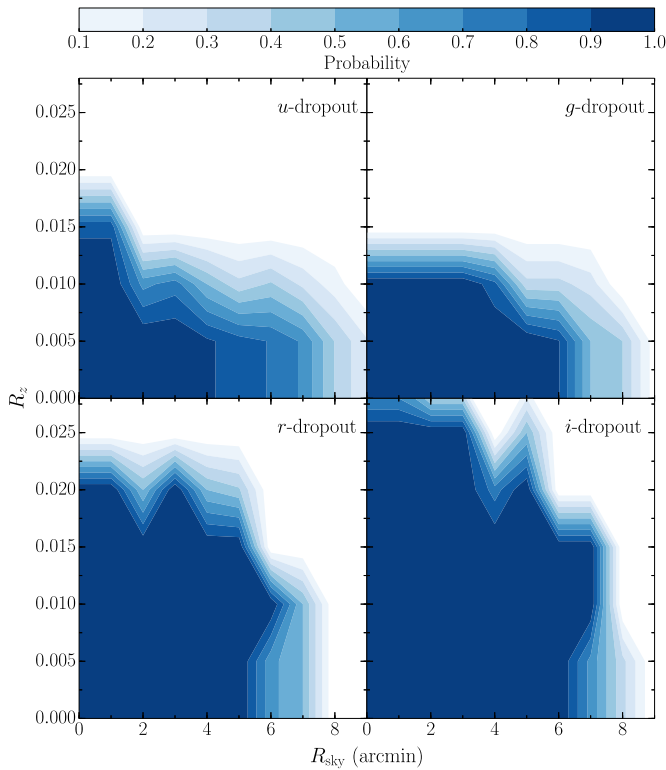


Figure 8. Probability of protocluster member as a function of distance from the center of a protocluster. The horizontal and vertical axes indicate spatial and redshift directions, and color contours show the probability. At $z = 3.0$ (5.9), 2 physical Mpc corresponds to $\Delta z = 0.009$ (0.032) and 4.3 (5.8) arcmin.

lower, and only three galaxies are clustering within the expected redshift range of the protocluster candidate ($\Delta z < 0.01$). Given the total number of confirmed galaxies in the overdense region, the group of three galaxies can be reproduced even from a random homogeneous distribution with a probability of 21%. Based on this probability, it cannot be dismissed that the observed redshift distribution is drawn from a uniform random distribution. Hence, we cannot currently conclude that there is a protocluster in the D1GD01 region without further observations. Hereafter, we regard the D1GD01 region as not being a protocluster. The high surface overdensity observed in this field could be attributed to a coincidental alignment of large-scale structure on a scale of $\Delta z \sim 0.1$ – 0.2 , which is too large to grow into a single halo by $z = 0$.

4.3.6. The g -Dropout Protocluster Candidate in the D4 Field

Combining the DEIMOS and FOCAS follow-up observations, 144 g -dropout galaxies were spectroscopically observed in the D4GD01 protocluster region, and the redshifts of 42 galaxies were determined by detecting Ly α emission lines. The sky distribution of the observed galaxies is shown in Figure 16. The redshift distribution is shown in Figure 17. There is a clear excess at $z = 3.67$, and, as contrasted with the D1GD01 region, 11 galaxies are clustered in a narrow redshift range of $\Delta z = 0.016$, corresponding to 2.6 Mpc in the physical scale. Since it is almost impossible ($< 0.01\%$) to explain this clustering with a random homogeneous distribution, we concluded that there is a protocluster at $z = 3.67$ that includes 11 member galaxies (ID = 10–20).

It should also be noted that an AGN was found in this region at $(\Delta R.A., \Delta \text{decl.}) = (-1.9, 6.8)$ arcmin by our spectroscopy, as shown in Figure 16. The redshift was derived to be $z = 3.72$ based on its He II and C III] emission lines (Figure 18). According to this estimate, the redshift separation between the AGN and the center of the protocluster is $\Delta z = 0.05$, which corresponds to the radial distance of ~ 8 physical Mpc. As the redshift separation is too large, it is unlikely that this AGN is a part of the protocluster members that will merge into a single halo by $z = 0$.

4.3.7. The u -Dropout Protocluster Candidate in the D1 Field

We have spectroscopically observed 95 u -dropout galaxies in the D1UD01 region, and 30 galaxies have single emission lines. The sky distribution of the observed galaxies is shown in Figure 19. The redshift distribution is shown in Figure 20. There is a excess at $z = 3.13$, including five galaxies within $\Delta z = 0.008$. The probability to reproduce this excess by drawing from a uniform random distribution of 30 galaxies is only 0.9%; thus, the five galaxies were found to be significantly clustered, though the absolute excess is only five. The spatial and redshift separations among these five galaxies are small enough to merge into a single halo by $z = 0$ compared with the model prediction; therefore we confirmed a protocluster at $z = 3.13$, which includes five member galaxies (ID = 6–10).

4.3.8. The u -Dropout Protocluster Candidate in the D4 Field

We have spectroscopically observed 57 u -dropout galaxies in the D4UD01 region, and 16 galaxies have single emission lines. The sky distribution of the observed galaxies

Table 3
Overview of Our Spectroscopic Observations

Date	Instrument	Target	Grism	Resolution (\AA)	Coverage (\AA)	t_{exp} (minutes)	N_{mask}	Seeing
2012 May 13 and 14	GMOS	D3ID01	R600	4.5	7500–10000	330	1	0".5
2012 Oct 21	FOCAS	D1ID01	VPH900	5.7	7500–10100	220	1	0".9
2014 Aug 24	DEIMOS	D1GD01	600ZD	3.5	5000–9300	120	1	0".7
		D4GD01	600ZD	3.5	5000–9300	120	1	0".7
2014 Oct 20 and 21	FOCAS	D1RD01	VPH650	5.5	6000–8300	280	1	0".7
		D1GD01	VPH520	2.5	4900–6500	100	1	0".9
		D1UD01	VPH520	2.5	4300–5900	60	4	0".6
		D4GD01	VPH520	2.5	4900–6500	120	2	0".7
2014 Oct 24 and 25	FOCAS	D4UD01	VPH520	2.5	4300–5900	60	3	0".8
		D4RD02	VPH650	5.5	6000–8300	120	1	0".8

Table 4
Observed Properties of All Spectroscopically Confirmed Dropout Galaxies

ID	R.A. (J2000)	decl. (J2000)	m^a (mag)	Redshift	M_{UV} (mag)	$f_{Ly\alpha}$ (10^{-18} erg s $^{-1}$ cm $^{-2}$)	$L_{Ly\alpha}$ (10^{42} erg s $^{-1}$)	EW_0 (Å)	$S_{3\gamma}$ (Å)
D11D01 (three galaxies)									
1	02:27:18.8	−04:50:08.3	25.45 ± 0.06	5.966 $^{+0.002}_{-0.004}$	−21.57 ± 0.06	2.66 ± 0.41	1.05 ± 0.16	2.41 ± 0.46	2.25 ± 1.21
2	02:27:21.0	−04:50:49.3	25.97 ± 0.10	6.044 $^{+0.002}_{-0.002}$	−20.85 ± 0.13	19.55 ± 0.72	7.92 ± 0.29	40.05 ± 6.13	5.21 ± 0.72
3	02:27:19.0	−04:53:48.0	26.30 ± 0.13	6.325 $^{+0.002}_{-0.003}$	−20.76 ± 0.24	31.73 ± 0.46	14.29 ± 0.21	81.79 ± 24.95	7.85 ± 0.59
D31D01 (two galaxies)									
1	14:19:22.5	+52:57:22.5	25.21 ± 0.05	5.749 $^{+0.002}_{-0.002}$	−21.49 ± 0.05	5.80 ± 0.88	2.09 ± 0.32	3.79 ± 0.84	5.41 ± 1.16
2	14:19:17.2	+52:56:14.4	25.74 ± 0.08	5.756 $^{+0.002}_{-0.002}$	−20.94 ± 0.08	8.16 ± 1.10	2.95 ± 0.40	10.84 ± 2.14	5.38 ± 3.85
D1RD01 (six galaxies)									
1	02:24:45.467	−04:58:52.83	26.37 ± 0.06	4.431 $^{+0.002}_{-0.002}$	−19.85 ± 0.14	1.60 ± 0.39	0.31 ± 0.08	4.09 ± 1.14	3.08 ± 5.41
2	02:24:45.957	−04:56:57.69	26.14 ± 0.05	4.602 $^{+0.002}_{-0.002}$	−20.14 ± 0.12	2.75 ± 0.46	0.59 ± 0.10	5.84 ± 1.17	0.72 ± 4.11
3	02:24:42.586	−04:58:36.00	26.81 ± 0.09	4.742 $^{+0.002}_{-0.003}$	−19.49 ± 0.21	5.22 ± 0.46	1.20 ± 0.10	21.69 ± 5.06	6.73 ± 2.10
4	02:24:38.212	−04:57:15.05	26.16 ± 0.05	4.840 $^{+0.002}_{-0.002}$	−20.21 ± 0.13	5.67 ± 0.73	1.37 ± 0.18	12.79 ± 2.28	15.74 ± 5.69
5	02:24:45.964	−04:54:34.80	26.12 ± 0.05	4.890 $^{+0.002}_{-0.002}$	−20.35 ± 0.12	1.73 ± 0.31	0.43 ± 0.08	3.52 ± 0.74	3.11 ± 2.06
6	02:24:43.757	−04:54:31.19	26.32 ± 0.05	4.894 $^{+0.002}_{-0.002}$	−20.19 ± 0.14	1.56 ± 0.29	0.39 ± 0.07	3.69 ± 0.85	0.58 ± 6.76
D4RD02 (three galaxies)									
1	22:16:46.722	−17:28:02.00	26.00 ± 0.05	4.630 $^{+0.002}_{-0.002}$	−20.27 ± 0.12	1.27 ± 0.17	0.28 ± 0.04	2.44 ± 0.43	3.47 ± 21.52
2	22:16:39.959	−17:31:34.58	25.94 ± 0.04	4.865 $^{+0.002}_{-0.002}$	−20.41 ± 0.12	10.31 ± 0.45	2.52 ± 0.11	19.51 ± 2.48	14.12 ± 2.55
3	22:16:45.765	−17:29:19.89	26.07 ± 0.05	4.952 $^{+0.004}_{-0.002}$	−20.36 ± 0.14	9.98 ± 0.35	2.54 ± 0.09	20.67 ± 2.93	15.00 ± 2.88
D1GD01 (36 galaxies)									
1	02:25:28.536	−04:17:14.12	26.93 ± 0.07	3.435 $^{+0.001}_{-0.001}$	−18.85 ± 0.15	12.50 ± 1.49	1.34 ± 0.16	43.82 ± 8.47	3.32 ± 8.74
2	02:25:30.408	−04:15:56.70	26.92 ± 0.07	3.623 $^{+0.001}_{-0.001}$	−18.92 ± 0.16	6.94 ± 0.92	0.84 ± 0.11	25.90 ± 5.31	2.74 ± 2.46
3	02:25:32.014	−04:17:03.56	27.17 ± 0.09	3.705 $^{+0.001}_{-0.001}$	−18.66 ± 0.21	6.85 ± 1.01	0.88 ± 0.13	34.18 ± 8.92	8.91 ± 4.93
4	02:25:25.565	−04:17:12.58	27.15 ± 0.09	3.717 $^{+0.001}_{-0.001}$	−18.73 ± 0.20	4.51 ± 0.90	0.58 ± 0.12	21.26 ± 6.04	1.08 ± 1.34
5	02:26:12.550	−04:18:41.23	26.69 ± 0.06	3.733 $^{+0.001}_{-0.001}$	−18.94 ± 0.17	21.41 ± 1.71	2.79 ± 0.22	83.76 ± 15.69	−0.32 ± 3.13
6	02:25:17.290	−04:14:02.23	25.40 ± 0.02	3.738 $^{+0.001}_{-0.001}$	−20.49 ± 0.04	21.57 ± 1.23	2.82 ± 0.16	20.45 ± 1.43	6.11 ± 0.86
7	02:25:51.739	−04:14:37.26	26.07 ± 0.03	3.744 $^{+0.001}_{-0.001}$	−19.91 ± 0.07	3.07 ± 0.79	0.40 ± 0.10	4.97 ± 1.32	0.23 ± 2.27
8	02:25:39.708	−04:14:20.73	25.22 ± 0.01	3.754 $^{+0.001}_{-0.001}$	−20.76 ± 0.04	9.32 ± 1.58	1.23 ± 0.21	6.97 ± 1.20	9.41 ± 9.42
9	02:26:11.563	−04:19:21.65	25.88 ± 0.03	3.755 $^{+0.001}_{-0.001}$	−19.82 ± 0.08	39.82 ± 2.21	5.27 ± 0.29	70.40 ± 6.78	8.13 ± 1.98
10	02:26:10.246	−04:18:18.50	26.81 ± 0.06	3.759 $^{+0.001}_{-0.001}$	−18.69 ± 0.21	25.61 ± 1.08	3.40 ± 0.14	128.41 ± 28.60	5.91 ± 0.54
11	02:25:33.011	−04:14:45.24	25.28 ± 0.02	3.766 $^{+0.001}_{-0.001}$	−20.53 ± 0.04	47.32 ± 2.23	6.30 ± 0.30	43.78 ± 2.74	12.15 ± 1.04
12	02:26:07.202	−04:17:12.22	26.73 ± 0.06	3.793 $^{+0.001}_{-0.001}$	−19.17 ± 0.15	9.89 ± 1.63	1.34 ± 0.22	32.77 ± 7.27	3.60 ± 4.24
13	02:25:59.907	−04:15:45.42	26.23 ± 0.04	3.797 $^{+0.001}_{-0.001}$	−19.74 ± 0.09	10.03 ± 2.29	1.36 ± 0.31	19.73 ± 4.83	7.09 ± 4.96
14	02:25:57.460	−04:18:10.27	26.01 ± 0.03	3.799 $^{+0.001}_{-0.001}$	−19.99 ± 0.07	7.82 ± 1.38	1.06 ± 0.19	12.24 ± 2.32	8.82 ± 4.36
15	02:25:42.923	−04:15:38.74	26.41 ± 0.04	3.800 $^{+0.001}_{-0.001}$	−19.44 ± 0.12	17.61 ± 1.24	2.40 ± 0.17	45.41 ± 6.08	9.85 ± 1.19
16	02:25:44.405	−04:14:11.81	25.32 ± 0.02	3.803 $^{+0.001}_{-0.001}$	−20.64 ± 0.04	24.22 ± 2.34	3.30 ± 0.32	20.78 ± 2.16	10.09 ± 2.61
17	02:25:34.147	−04:14:21.23	26.40 ± 0.04	3.809 $^{+0.001}_{-0.001}$	−19.59 ± 0.11	8.27 ± 1.39	1.13 ± 0.19	18.65 ± 3.66	6.15 ± 4.06
18	02:25:56.529	−04:17:27.85	26.77 ± 0.06	3.818 $^{+0.001}_{-0.001}$	−19.15 ± 0.16	10.76 ± 1.85	1.48 ± 0.25	36.77 ± 8.52	3.17 ± 8.69
19	02:25:30.087	−04:15:15.84	25.85 ± 0.03	3.827 $^{+0.001}_{-0.001}$	−20.20 ± 0.06	6.02 ± 0.94	0.83 ± 0.13	7.83 ± 1.30	8.59 ± 1.02
20	02:25:49.845	−04:14:53.42	26.57 ± 0.05	3.829 $^{+0.001}_{-0.001}$	−19.35 ± 0.13	13.03 ± 1.37	1.81 ± 0.19	37.33 ± 6.22	13.66 ± 4.39
21	02:25:41.772	−04:16:06.53	25.70 ± 0.02	3.843 $^{+0.002}_{-0.001}$	−20.30 ± 0.06	21.31 ± 1.34	2.98 ± 0.19	25.65 ± 2.14	−0.62 ± 0.96
22	02:25:56.593	−04:15:15.20	26.89 ± 0.07	3.859 $^{+0.001}_{-0.001}$	−18.85 ± 0.21	19.31 ± 1.22	2.73 ± 0.17	88.80 ± 19.46	5.15 ± 0.78

Table 4
(Continued)

ID	R.A. (J2000)	decl. (J2000)	m^a (mag)	Redshift	M_{UV} (mag)	$f_{Ly\alpha}$ (10^{-18} erg s $^{-1}$ cm $^{-2}$)	$L_{Ly\alpha}$ (10^{42} erg s $^{-1}$)	EW_0 (Å)	S_{ν} (Å)
23	02:25:39.324	-04:14:40.82	26.79 ± 0.06	3.866 $^{+0.001}_{-0.001}$	-19.12 ± 0.17	13.16 ± 1.11	1.87 ± 0.16	47.68 ± 8.84	5.37 ± 0.92
24	02:26:11.555	-04:17:39.51	26.38 ± 0.04	3.886 $^{+0.001}_{-0.001}$	-19.35 ± 0.14	33.92 ± 2.51	4.87 ± 0.36	100.23 ± 15.93	1.63 ± 1.82
25	02:25:27.362	-04:16:43.59	27.28 ± 0.10	3.891 $^{+0.001}_{-0.001}$	-18.37 ± 0.32	17.16 ± 1.63	2.47 ± 0.24	125.83 ± 44.70	2.87 ± 0.77
26	02:25:25.816	-04:16:38.94	27.61 ± 0.13	3.927 $^{+0.001}_{-0.001}$	-18.04 ± 0.43	13.14 ± 1.83	1.93 ± 0.27	133.94 ± 67.59	-1.16 ± 6.97
27	02:26:01.853	-04:14:41.24	27.73 ± 0.15	4.000 $^{+0.001}_{-0.001}$	-17.65 ± 0.61	15.71 ± 2.24	2.41 ± 0.34	238.11 ± 183.28	5.40 ± 1.71
28	02:25:31.239	-04:15:49.81	26.37 ± 0.04	4.054 $^{+0.001}_{-0.001}$	-19.76 ± 0.12	18.39 ± 1.82	2.92 ± 0.29	41.22 ± 6.28	5.63 ± 2.24
29	02:25:35.470	-04:14:15.68	26.25 ± 0.04	4.119 $^{+0.001}_{-0.001}$	-19.94 ± 0.11	23.18 ± 1.90	3.82 ± 0.31	45.59 ± 6.16	3.35 ± 4.05
30	02:25:34.433	-04:15:05.46	26.37 ± 0.04	4.185 $^{+0.001}_{-0.001}$	-19.83 ± 0.13	25.45 ± 1.46	4.35 ± 0.25	57.91 ± 8.23	8.31 ± 0.57
31	02:25:39.830	-04:14:53.33	26.20 ± 0.04	4.236 $^{+0.001}_{-0.002}$	-20.19 ± 0.11	23.32 ± 2.01	4.11 ± 0.35	39.12 ± 5.27	6.86 ± 1.12
32	02:25:11.525	-04:16:20.17	25.91 ± 0.03	4.276 $^{+0.001}_{-0.001}$	-19.10 ± 0.29	107.86 ± 2.43	19.42 ± 0.44	505.39 ± 153.02	2.40 ± 0.33
33	02:25:57.659	-04:14:24.90	26.54 ± 0.05	4.385 $^{+0.001}_{-0.001}$	-18.83 ± 0.40	61.69 ± 2.19	11.79 ± 0.42	393.36 ± 177.53	5.26 ± 0.81
34	02:25:21.473	-04:16:01.50	27.04 ± 0.08	4.391 $^{+0.001}_{-0.002}$	-19.20 ± 0.30	23.76 ± 2.33	4.55 ± 0.45	107.90 ± 36.20	5.27 ± 1.87
35	02:25:08.716	-04:15:24.74	27.10 ± 0.08	4.395 $^{+0.001}_{-0.001}$	-19.34 ± 0.27	52.76 ± 2.69	10.13 ± 0.52	210.28 ± 60.76	7.74 ± 0.99
36	02:25:28.097	-04:14:54.46	27.68 ± 0.14	4.442 $^{+0.001}_{-0.001}$	-18.01 ± 0.78	22.59 ± 2.06	4.45 ± 0.41	316.27 ± 334.36	4.13 ± 1.99
D4GD01 (42 galaxies)									
1	22:16:55.191	-17:25:51.91	24.53 ± 0.01	3.568 $^{+0.001}_{-0.001}$	-21.32 ± 0.02	11.47 ± 1.23	1.34 ± 0.14	4.54 ± 0.50	7.39 ± 2.56
2	22:17:00.190	-17:25:06.37	26.39 ± 0.05	3.569 $^{+0.001}_{-0.001}$	-19.45 ± 0.11	9.05 ± 1.27	1.06 ± 0.15	20.01 ± 3.48	4.83 ± 1.81
3	22:16:55.670	-17:20:49.98	27.16 ± 0.10	3.581 $^{+0.001}_{-0.001}$	-18.67 ± 0.21	6.39 ± 0.65	0.76 ± 0.08	29.05 ± 6.79	1.78 ± 1.80
4	22:16:49.872	-17:21:53.02	25.42 ± 0.02	3.622 $^{+0.001}_{-0.001}$	-20.44 ± 0.05	14.01 ± 1.24	1.70 ± 0.15	12.85 ± 1.26	5.97 ± 4.29
5	22:17:01.326	-17:20:52.55	26.81 ± 0.07	3.624 $^{+0.001}_{-0.001}$	-19.04 ± 0.15	5.40 ± 1.15	0.66 ± 0.14	17.95 ± 4.70	-0.73 ± 2.60
6	22:16:54.811	-17:28:37.91	26.93 ± 0.08	3.626 $^{+0.001}_{-0.001}$	-18.89 ± 0.18	10.59 ± 1.15	1.29 ± 0.14	40.75 ± 8.47	3.86 ± 1.26
7	22:16:58.872	-17:28:33.27	26.33 ± 0.04	3.628 $^{+0.001}_{-0.001}$	-19.53 ± 0.10	6.92 ± 1.32	0.84 ± 0.16	14.68 ± 3.15	5.65 ± 3.60
8	22:17:07.296	-17:28:45.15	26.22 ± 0.04	3.654 $^{+0.001}_{-0.001}$	-19.61 ± 0.10	16.61 ± 1.61	2.06 ± 0.20	33.43 ± 4.49	4.80 ± 3.23
9	22:16:51.756	-17:24:57.97	26.26 ± 0.04	3.666 $^{+0.001}_{-0.001}$	-19.59 ± 0.10	11.90 ± 0.89	1.49 ± 0.11	24.67 ± 3.00	1.03 ± 2.79
10	22:16:42.993	-17:15:53.36	26.96 ± 0.08	3.669 $^{+0.001}_{-0.001}$	-18.90 ± 0.18	4.98 ± 0.89	0.62 ± 0.11	19.56 ± 4.98	7.49 ± 2.83
11	22:16:50.981	-17:18:49.87	26.71 ± 0.06	3.670 $^{+0.001}_{-0.001}$	-19.10 ± 0.15	11.16 ± 2.01	1.40 ± 0.25	36.23 ± 8.51	5.17 ± 4.24
12	22:16:53.509	-17:19:06.60	25.74 ± 0.03	3.671 $^{+0.001}_{-0.001}$	-20.08 ± 0.06	23.63 ± 1.76	2.96 ± 0.22	31.08 ± 2.99	5.67 ± 2.85
13	22:16:49.716	-17:17:00.96	26.45 ± 0.05	3.671 $^{+0.001}_{-0.001}$	-19.41 ± 0.12	8.69 ± 1.12	1.09 ± 0.14	21.37 ± 3.67	7.45 ± 1.80
14	22:16:53.576	-17:19:07.20	24.96 ± 0.01	3.671 $^{+0.001}_{-0.001}$	-20.92 ± 0.03	17.97 ± 1.17	2.25 ± 0.15	10.92 ± 0.77	14.77 ± 4.05
15	22:16:51.410	-17:17:50.44	26.02 ± 0.03	3.672 $^{+0.001}_{-0.001}$	-19.83 ± 0.08	14.83 ± 1.31	1.86 ± 0.16	24.75 ± 2.90	4.22 ± 1.98
16	22:16:54.326	-17:18:34.98	25.95 ± 0.03	3.675 $^{+0.001}_{-0.001}$	-19.95 ± 0.07	6.62 ± 0.81	0.83 ± 0.10	9.85 ± 1.39	5.83 ± 2.25
17	22:16:57.890	-17:21:51.88	26.42 ± 0.05	3.675 $^{+0.001}_{-0.001}$	-19.37 ± 0.12	18.62 ± 1.19	2.34 ± 0.15	47.33 ± 6.39	4.28 ± 0.83
18	22:16:51.591	-17:18:12.00	26.30 ± 0.04	3.681 $^{+0.001}_{-0.001}$	-19.61 ± 0.10	4.78 ± 0.95	0.60 ± 0.12	9.83 ± 2.17	4.43 ± 2.62
19	22:16:55.554	-17:20:14.08	26.66 ± 0.06	3.681 $^{+0.001}_{-0.001}$	-19.14 ± 0.15	12.33 ± 1.31	1.55 ± 0.17	38.80 ± 7.05	5.73 ± 2.17
20	22:16:48.909	-17:15:31.09	26.51 ± 0.05	3.685 $^{+0.001}_{-0.001}$	-19.35 ± 0.12	8.96 ± 1.38	1.13 ± 0.17	23.36 ± 4.59	-3.55 ± 6.95
21	22:16:55.005	-17:21:00.75	25.78 ± 0.03	3.717 $^{+0.001}_{-0.001}$	-20.06 ± 0.07	22.37 ± 1.51	2.89 ± 0.19	31.09 ± 2.93	9.26 ± 1.83
22	22:16:46.962	-17:21:06.42	25.93 ± 0.03	3.719 $^{+0.001}_{-0.001}$	-19.74 ± 0.09	41.34 ± 1.66	5.35 ± 0.21	77.34 ± 7.55	5.17 ± 0.88
23	22:16:46.961	-17:17:10.24	27.19 ± 0.10	3.720 $^{+0.001}_{-0.001}$	-18.64 ± 0.24	6.30 ± 0.94	0.81 ± 0.12	32.32 ± 9.19	3.09 ± 2.67
24	22:16:42.903	-17:17:35.09	25.47 ± 0.02	3.721 $^{+0.001}_{-0.001}$	-20.44 ± 0.05	14.86 ± 1.46	1.92 ± 0.19	14.53 ± 1.58	2.22 ± 2.25
25	22:16:50.522	-17:18:22.62	26.00 ± 0.03	3.723 $^{+0.001}_{-0.001}$	-19.87 ± 0.08	15.39 ± 1.44	2.00 ± 0.19	25.62 ± 3.13	11.86 ± 2.51
26	22:16:49.533	-17:16:44.13	26.38 ± 0.05	3.728 $^{+0.001}_{-0.001}$	-19.50 ± 0.11	8.94 ± 1.05	1.16 ± 0.14	20.82 ± 3.35	10.33 ± 3.45
27	22:17:09.126	-17:28:52.31	26.73 ± 0.06	3.730 $^{+0.001}_{-0.001}$	-19.07 ± 0.17	11.89 ± 1.54	1.55 ± 0.20	41.26 ± 8.65	3.25 ± 1.57

Table 4
(Continued)

ID	R.A. (J2000)	decl. (J2000)	m^a (mag)	Redshift	M_{UV} (mag)	$f_{Ly\alpha}$ (10^{-18} erg s $^{-1}$ cm $^{-2}$)	$L_{Ly\alpha}$ (10^{42} erg s $^{-1}$)	EW_0 (Å)	S_{ν} (Å)
28	22:16:56.467	-17:17:20.11	26.68 ± 0.06	3.831 $^{+0.001}_{-0.001}$	-19.12 ± 0.17	19.18 ± 0.72	2.66 ± 0.10	67.69 ± 11.99	4.13 ± 0.77
29	22:17:01.475	-17:23:58.97	27.01 ± 0.08	3.837 $^{+0.001}_{-0.001}$	-18.82 ± 0.23	13.81 ± 1.17	1.92 ± 0.16	64.73 ± 16.19	5.90 ± 1.67
30	22:17:04.114	-17:29:22.86	26.57 ± 0.06	3.839 $^{+0.001}_{-0.001}$	-19.29 ± 0.16	19.06 ± 1.23	2.66 ± 0.17	58.23 ± 9.70	3.59 ± 1.20
31	22:16:59.785	-17:26:15.22	25.50 ± 0.02	3.852 $^{+0.001}_{-0.003}$	-20.57 ± 0.05	12.90 ± 1.35	1.81 ± 0.19	12.16 ± 1.40	4.41 ± 1.16
32	22:17:00.167	-17:27:32.72	26.70 ± 0.06	3.854 $^{+0.001}_{-0.001}$	-19.03 ± 0.19	23.89 ± 1.47	3.36 ± 0.21	93.40 ± 19.22	3.68 ± 2.03
33	22:16:44.680	-17:17:48.48	25.93 ± 0.03	3.856 $^{+0.001}_{-0.001}$	-19.49 ± 0.13	75.34 ± 1.29	10.62 ± 0.18	192.60 ± 24.90	1.53 ± 0.42
34	22:16:49.846	-17:17:16.49	26.41 ± 0.05	4.026 $^{+0.001}_{-0.001}$	-19.11 ± 0.22	48.03 ± 2.06	7.50 ± 0.32	193.21 ± 43.99	8.03 ± 0.93
35	22:16:51.997	-17:26:10.95	25.85 ± 0.03	4.076 $^{+0.001}_{-0.001}$	-20.35 ± 0.08	27.36 ± 1.87	4.40 ± 0.30	36.05 ± 3.71	5.22 ± 1.24
36	22:16:53.458	-17:20:03.45	27.06 ± 0.09	4.093 $^{+0.001}_{-0.001}$	-19.19 ± 0.22	7.49 ± 0.66	1.22 ± 0.11	29.18 ± 6.98	7.24 ± 1.49
37	22:16:52.593	-17:29:00.63	26.89 ± 0.08	4.109 $^{+0.001}_{-0.001}$	-19.17 ± 0.23	17.48 ± 1.22	2.86 ± 0.20	70.02 ± 17.27	5.76 ± 1.73
38	22:16:59.778	-17:22:16.93	25.75 ± 0.03	4.126 $^{+0.001}_{-0.001}$	-20.12 ± 0.11	68.15 ± 2.28	11.28 ± 0.38	115.08 ± 12.30	4.28 ± 0.67
39	22:17:03.102	-17:25:52.33	25.23 ± 0.02	4.170 $^{+0.001}_{-0.001}$	-20.63 ± 0.07	120.44 ± 3.00	20.43 ± 0.51	130.16 ± 9.74	11.81 ± 0.64
40	22:16:48.708	-17:15:41.17	26.41 ± 0.05	4.182 $^{+0.002}_{-0.001}$	-19.79 ± 0.15	25.01 ± 1.35	4.27 ± 0.23	59.09 ± 9.28	1.45 ± 0.88
41	22:16:49.635	-17:15:26.63	27.50 ± 0.13	4.220 $^{+0.001}_{-0.001}$	-18.24 ± 0.54	17.35 ± 1.48	3.03 ± 0.26	173.91 ± 113.30	6.64 ± 1.53
42	22:16:56.050	-17:24:57.12	26.65 ± 0.06	4.258 $^{+0.001}_{-0.001}$	-19.59 ± 0.19	22.63 ± 1.57	4.03 ± 0.28	66.48 ± 13.79	6.99 ± 1.76
DIUD01 (30 galaxies)									
1	02:24:33.775	-04:22:05.64	27.48 ± 0.08	2.730 $^{+0.001}_{-0.001}$	-17.14 ± 0.33	36.73 ± 4.16	2.26 ± 0.26	357.30 ± 132.78	6.12 ± 1.92
2	02:24:24.047	-04:19:30.14	26.75 ± 0.04	2.936 $^{+0.001}_{-0.001}$	-18.82 ± 0.09	11.49 ± 1.98	0.84 ± 0.15	28.27 ± 5.46	5.96 ± 3.75
3	02:24:38.501	-04:19:31.91	25.96 ± 0.02	2.954 $^{+0.001}_{-0.001}$	-19.63 ± 0.04	24.14 ± 1.82	1.80 ± 0.14	28.80 ± 2.48	5.79 ± 1.33
4	02:24:32.251	-04:20:05.64	26.36 ± 0.03	2.961 $^{+0.001}_{-0.001}$	-19.18 ± 0.07	24.91 ± 1.67	1.87 ± 0.13	45.24 ± 4.18	10.26 ± 1.40
5	02:24:30.247	-04:20:25.53	24.45 ± 0.01	2.977 $^{+0.001}_{-0.001}$	-21.21 ± 0.01	52.64 ± 3.69	3.99 ± 0.28	14.85 ± 1.05	11.87 ± 1.47
6	02:24:35.414	-04:20:32.25	26.00 ± 0.02	3.124 $^{+0.001}_{-0.001}$	-19.61 ± 0.05	58.84 ± 2.09	5.01 ± 0.18	81.48 ± 5.02	8.38 ± 1.17
7	02:24:32.181	-04:18:52.41	27.00 ± 0.05	3.127 $^{+0.001}_{-0.001}$	-18.75 ± 0.12	11.77 ± 2.07	1.01 ± 0.18	36.17 ± 7.54	12.53 ± 5.35
8	02:24:26.931	-04:18:09.40	25.10 ± 0.01	3.130 $^{+0.001}_{-0.001}$	-20.77 ± 0.02	16.28 ± 1.97	1.39 ± 0.17	7.81 ± 0.95	1.18 ± 1.96
9	02:24:32.111	-04:19:01.04	26.73 ± 0.04	3.131 $^{+0.001}_{-0.001}$	-19.09 ± 0.09	9.38 ± 1.71	0.80 ± 0.15	21.03 ± 4.21	7.64 ± 2.41
10	02:24:32.361	-04:18:33.93	27.32 ± 0.07	3.132 $^{+0.001}_{-0.001}$	-18.45 ± 0.15	8.49 ± 1.34	0.73 ± 0.12	34.32 ± 7.41	0.35 ± 3.73
11	02:24:38.052	-04:17:50.69	25.76 ± 0.02	3.150 $^{+0.001}_{-0.001}$	-20.08 ± 0.04	18.81 ± 2.10	1.64 ± 0.18	17.21 ± 2.00	6.70 ± 2.73
12	02:24:36.424	-04:20:40.01	27.41 ± 0.08	3.193 $^{+0.001}_{-0.001}$	-18.27 ± 0.18	17.26 ± 1.44	1.55 ± 0.13	86.42 ± 17.51	-1.63 ± 4.53
13	02:24:39.007	-04:17:25.43	26.14 ± 0.02	3.200 $^{+0.001}_{-0.001}$	-19.77 ± 0.05	14.54 ± 1.65	1.31 ± 0.15	18.37 ± 2.25	6.27 ± 1.62
14	02:24:35.609	-04:19:31.99	27.32 ± 0.07	3.220 $^{+0.001}_{-0.001}$	-18.46 ± 0.16	14.64 ± 1.81	1.34 ± 0.17	62.97 ± 12.76	3.07 ± 2.45
15	02:24:36.250	-04:19:11.89	25.81 ± 0.02	3.258 $^{+0.001}_{-0.001}$	-20.04 ± 0.04	56.13 ± 2.21	5.29 ± 0.21	57.99 ± 3.23	12.49 ± 1.98
16	02:24:36.988	-04:18:09.47	25.44 ± 0.01	3.274 $^{+0.002}_{-0.001}$	-20.53 ± 0.03	42.95 ± 2.36	4.10 ± 0.23	28.53 ± 1.73	14.83 ± 2.07
17	02:24:27.725	-04:17:48.50	27.03 ± 0.06	3.284 $^{+0.001}_{-0.001}$	-18.83 ± 0.13	20.07 ± 1.68	1.93 ± 0.16	64.53 ± 9.60	5.80 ± 1.54
18	02:24:35.157	-04:17:00.64	26.61 ± 0.04	3.344 $^{+0.001}_{-0.001}$	-19.48 ± 0.08	8.56 ± 1.33	0.86 ± 0.13	15.65 ± 2.68	7.98 ± 2.43
19	02:24:28.399	-04:20:01.41	26.27 ± 0.03	3.351 $^{+0.001}_{-0.001}$	-19.77 ± 0.06	23.60 ± 1.80	2.38 ± 0.18	33.30 ± 3.16	10.49 ± 1.71
20	02:24:38.367	-04:17:16.11	27.34 ± 0.07	3.357 $^{+0.001}_{-0.001}$	-18.71 ± 0.15	7.92 ± 1.12	0.80 ± 0.11	29.73 ± 6.09	3.94 ± 1.62
21	02:24:41.996	-04:18:59.15	27.01 ± 0.05	3.400 $^{+0.001}_{-0.001}$	-19.11 ± 0.11	12.78 ± 1.57	1.33 ± 0.16	34.43 ± 5.69	10.15 ± 2.55
22	02:24:37.488	-04:19:20.22	26.12 ± 0.02	3.426 $^{+0.001}_{-0.001}$	-20.02 ± 0.05	34.92 ± 1.95	3.71 ± 0.21	41.50 ± 3.12	9.26 ± 0.97
23	02:24:28.416	-04:21:30.12	26.78 ± 0.04	3.435 $^{+0.001}_{-0.001}$	-19.32 ± 0.10	23.86 ± 1.70	2.55 ± 0.18	54.13 ± 6.44	3.95 ± 0.73
24	02:24:36.548	-04:18:26.31	26.56 ± 0.04	3.454 $^{+0.001}_{-0.001}$	-19.61 ± 0.08	21.02 ± 1.16	2.28 ± 0.13	37.07 ± 3.42	7.23 ± 1.34
25	02:24:35.602	-04:16:54.03	27.31 ± 0.07	3.455 $^{+0.001}_{-0.001}$	-18.60 ± 0.19	26.89 ± 1.59	2.92 ± 0.17	119.80 ± 23.53	3.58 ± 1.71
26	02:24:44.626	-04:19:35.65	26.24 ± 0.03	3.463 $^{+0.001}_{-0.001}$	-19.95 ± 0.06	30.63 ± 1.60	3.34 ± 0.17	39.74 ± 3.03	7.64 ± 2.19

Table 4
(Continued)

ID	R.A. (J2000)	decl. (J2000)	m^a (mag)	Redshift	M_{UV} (mag)	$f_{Ly\alpha}$ (10^{-18} erg s $^{-1}$ cm $^{-2}$)	$L_{Ly\alpha}$ (10^{42} erg s $^{-1}$)	EW_0 (Å)	S_{y^*} (Å)
27	02:24:38.037	-04:22:12.46	27.49 ± 0.08	3.529 $^{+0.001}_{-0.001}$	-18.67 ± 0.19	20.88 ± 1.47	2.38 ± 0.17	91.63 ± 19.14	9.51 ± 2.56
28	02:24:29.531	-04:21:43.03	26.83 ± 0.05	3.550 $^{+0.001}_{-0.001}$	-19.45 ± 0.10	29.51 ± 2.19	3.41 ± 0.25	64.39 ± 8.00	3.44 ± 2.08
29	02:24:35.608	-04:21:10.87	27.10 ± 0.06	3.551 $^{+0.001}_{-0.001}$	-19.25 ± 0.12	14.71 ± 1.57	1.70 ± 0.18	38.72 ± 6.21	11.86 ± 3.78
30	02:24:24.653	-04:19:31.71	26.99 ± 0.05	3.555 $^{+0.001}_{-0.001}$	-19.40 ± 0.11	11.07 ± 1.24	1.29 ± 0.14	25.39 ± 3.88	3.50 ± 3.09
D4UD01 (16 galaxies)									
1	22:14:03.642	-18:00:09.90	26.61 ± 0.04	2.973 $^{+0.001}_{-0.001}$	-19.05 ± 0.08	6.08 ± 1.27	0.46 ± 0.10	12.47 ± 2.79	3.65 ± 6.22
2	22:13:58.570	-17:59:30.91	27.05 ± 0.06	3.008 $^{+0.001}_{-0.001}$	-18.60 ± 0.13	7.66 ± 1.28	0.60 ± 0.10	24.50 ± 5.14	0.09 ± 1.53
3	22:14:11.265	-17:59:56.51	25.84 ± 0.02	3.037 $^{+0.001}_{-0.001}$	-19.70 ± 0.05	57.83 ± 2.77	4.61 ± 0.22	68.72 ± 4.69	7.67 ± 0.97
4	22:13:53.488	-17:56:54.74	26.56 ± 0.04	3.046 $^{+0.001}_{-0.001}$	-18.95 ± 0.10	33.35 ± 2.43	2.67 ± 0.19	80.04 ± 9.72	5.06 ± 1.72
5	22:13:51.171	-17:57:18.84	26.66 ± 0.04	3.138 $^{+0.001}_{-0.001}$	-19.15 ± 0.09	11.14 ± 1.56	0.96 ± 0.13	23.74 ± 3.92	4.81 ± 1.76
6	22:13:53.773	-17:57:40.48	27.09 ± 0.06	3.210 $^{+0.001}_{-0.001}$	-18.79 ± 0.13	9.29 ± 1.75	0.84 ± 0.16	29.27 ± 6.72	4.17 ± 1.95
7	22:13:54.597	-17:59:06.04	26.79 ± 0.05	3.241 $^{+0.001}_{-0.001}$	-19.12 ± 0.10	13.84 ± 1.33	1.29 ± 0.12	32.89 ± 4.58	2.97 ± 4.01
8	22:13:55.114	-17:59:55.62	26.26 ± 0.03	3.242 $^{+0.001}_{-0.001}$	-19.68 ± 0.06	16.00 ± 1.44	1.49 ± 0.13	22.77 ± 2.46	3.70 ± 2.06
9	22:14:04.835	-17:57:44.20	26.93 ± 0.06	3.243 $^{+0.001}_{-0.001}$	-18.81 ± 0.14	27.86 ± 1.96	2.60 ± 0.18	88.14 ± 13.39	9.82 ± 1.41
10	22:14:04.154	-18:00:05.58	26.72 ± 0.05	3.243 $^{+0.001}_{-0.001}$	-19.11 ± 0.11	23.82 ± 1.90	2.22 ± 0.18	56.94 ± 7.36	7.18 ± 1.45
11	22:14:03.430	-17:59:22.71	26.03 ± 0.02	3.249 $^{+0.001}_{-0.001}$	-19.90 ± 0.05	24.84 ± 1.88	2.32 ± 0.18	28.98 ± 2.62	5.89 ± 1.17
12	22:14:09.396	-17:57:58.56	26.98 ± 0.06	3.336 $^{+0.001}_{-0.001}$	-19.12 ± 0.11	3.32 ± 0.73	0.33 ± 0.07	8.44 ± 2.09	4.28 ± 10.94
13	22:14:16.330	-17:57:22.22	27.54 ± 0.10	3.341 $^{+0.001}_{-0.001}$	-18.46 ± 0.21	9.19 ± 1.56	0.92 ± 0.16	43.24 ± 11.65	6.27 ± 2.88
14	22:14:09.371	-17:58:15.61	26.99 ± 0.06	3.341 $^{+0.001}_{-0.001}$	-19.02 ± 0.13	13.93 ± 1.74	1.39 ± 0.17	39.00 ± 6.87	4.65 ± 2.26
15	22:13:58.117	-17:59:46.75	26.92 ± 0.06	3.560 $^{+0.001}_{-0.001}$	-19.48 ± 0.11	12.41 ± 1.54	1.44 ± 0.18	26.50 ± 4.40	5.63 ± 1.58
16	22:14:07.173	-18:00:24.05	26.48 ± 0.04	3.635 $^{+0.001}_{-0.001}$	-20.03 ± 0.08	37.94 ± 2.08	4.65 ± 0.26	51.22 ± 4.73	8.40 ± 1.04

Note.

^a The apparent aperture magnitude of detection band is i' band for u -, g -, and r -dropout, and z' band for i -dropout galaxies.

Table 5
Results of the Protocluster Confirmation

Name	$N_{\text{obs}}^{\text{a}}$	$N_{\text{det}}^{\text{b}}$	Protocluster?	$N_{\text{member}}^{\text{c}}$	Redshift	σ_v (km s $^{-1}$)
D1ID01	8	3	unclear
D3ID01	8	2	possible	2	5.75	...
D1RD01	15	6	possible	2	4.89	...
D4RD02	12	3	unclear
D1GD01	123	36	No
D4GD01	144	42	Yes	11	3.67	352 ± 140
D1UD01	95	30	Yes	5	3.13	235 ± 75
D4UD01	57	16	Yes	5	3.24	61 ± 105

Notes.

^a Number of observed galaxies.

^b Number of spectroscopically detected galaxies.

^c Number of protocluster members.

is shown in Figure 21. The redshift distribution is shown in Figure 22. There is a peak at $z = 3.24$, consisting of five galaxies within $\Delta z = 0.008$. The probability to reproduce this excess by a uniform random distribution of 16 galaxies was found to be less than 0.1%. These five galaxies are expected to merge into a single halo by $z = 0$ compared with the model prediction. Therefore, we confirmed a protocluster at $z = 3.24$, which includes five member galaxies (ID = 7–11).

4.3.9. Summary of Protocluster Confirmation

Based on these follow-up spectroscopic observations, we were able to confirm three protoclusters in the D4GD01, D1UD01, and D4UD01 regions. We could not confirm that the overdensity observed in the D1GD01 region is indeed a protocluster. Thus, at least, the success rate of our protocluster search is found to be 3/4 at $z \sim 3\text{--}4$, which is consistent with that of the model prediction ($\gtrsim 76\%$ of 4σ overdense regions are expected to be real protoclusters). As for r - and i -dropout protocluster candidates, it is unclear whether they are real protoclusters or not because of the small number of spectroscopically confirmed galaxies, though the D3ID01 and D1RD01 regions include close galaxy pairs, which could indicate the existence of protoclusters. These results suggest that most of the other protocluster candidates will turn out to be genuine protoclusters once sufficient follow-up spectroscopic observations are performed. The summary of our protocluster confirmation is described in Table 5. These findings not only increase the number of known protoclusters at high redshift, but also provide us with samples that are complementary to previous works in which protoclusters were mainly discovered in QSO or RG regions. Although we discovered one AGN in an overdense region by our spectroscopy, it was not associated with any protocluster. The precise relation between protoclusters and AGNs merits future investigation.

The radial velocity dispersions of the confirmed protoclusters were calculated by the redshifts of protocluster members assuming that the redshifts probe line-of-sight velocity. To calculate dispersion, we used the biweight variance (Beers et al. 1990), which is an effective method even with a small sample. Since our follow-up spectroscopy is not complete, the effect of small-number statistics should be taken into account in the uncertainty of the radial velocity dispersion. The uncertainty of the radial velocity dispersion was measured by the

combination of the velocity error of our spectroscopic observations and the standard deviation of the measurements by bootstrap sampling the protocluster members. In addition to the optical imaging and our spectroscopy, rich multiwavelength data are available in part of the CFHTLS Deep Fields. Although this enables us to do further analysis, such as SED fitting, to derive galaxy properties in more detail, these studies will be addressed in a future paper.

5. DISCUSSION

The D4GD01 protocluster, of which we confirmed 11 protocluster members, is the most extensively mapped protocluster among the three confirmed systems described in Section 4. Thus, we focus on this protocluster in the following discussion of the internal structure of the protocluster and the properties of its galaxies.

5.1. Protocluster Internal Structure

We investigated the three-dimensional distribution of protocluster galaxies in the D4GD01 region, as shown in Figure 23. In this analysis, the distances are simply estimated from the measured redshift, including any possible peculiar velocity component. However, we have checked that this does not significantly affect our estimates given the typical size of protoclusters.⁹ This protocluster seems to have a region where galaxies are strongly concentrated, reminiscent of a cluster core. To discuss the internal structure quantitatively, we calculated the spatial separation of galaxies with respect to the N th nearest neighbor. In Figure 24, the distributions of the separation from the first to sixth nearest galaxies of individual protocluster galaxies are shown, and the red-line histograms indicate the expected distribution if 11 galaxies are randomly located inside the protocluster. The distribution of protocluster galaxies from the third to fifth nearest are significantly different from the random distribution, whose significances are $p < 0.05$ based on the Kolmogorov–Smirnov (KS) test;

⁹ In principle, redshift does not completely correspond to radial distance, due to the effect of radial velocity. However, in the high-redshift protoclusters, nearly all of the member galaxies, which merge into a single dark matter halo with mass of $>10^{14} M_{\odot}$ by $z = 0$, are still embedded in individual host halos at $z > 3$, and their clustering is probably not strong enough to provoke a large peculiar velocity field. Therefore, we expect that their real three-dimensional distribution at some level can be determined by using their redshifts as proxies for their relative line-of-sight distances. According to the theoretical model of Henriques et al. (2012), the deviation of the difference between apparent and geometrical redshift is $\Delta z \sim 0.002$, shown by the black scale bar in Figure 23.

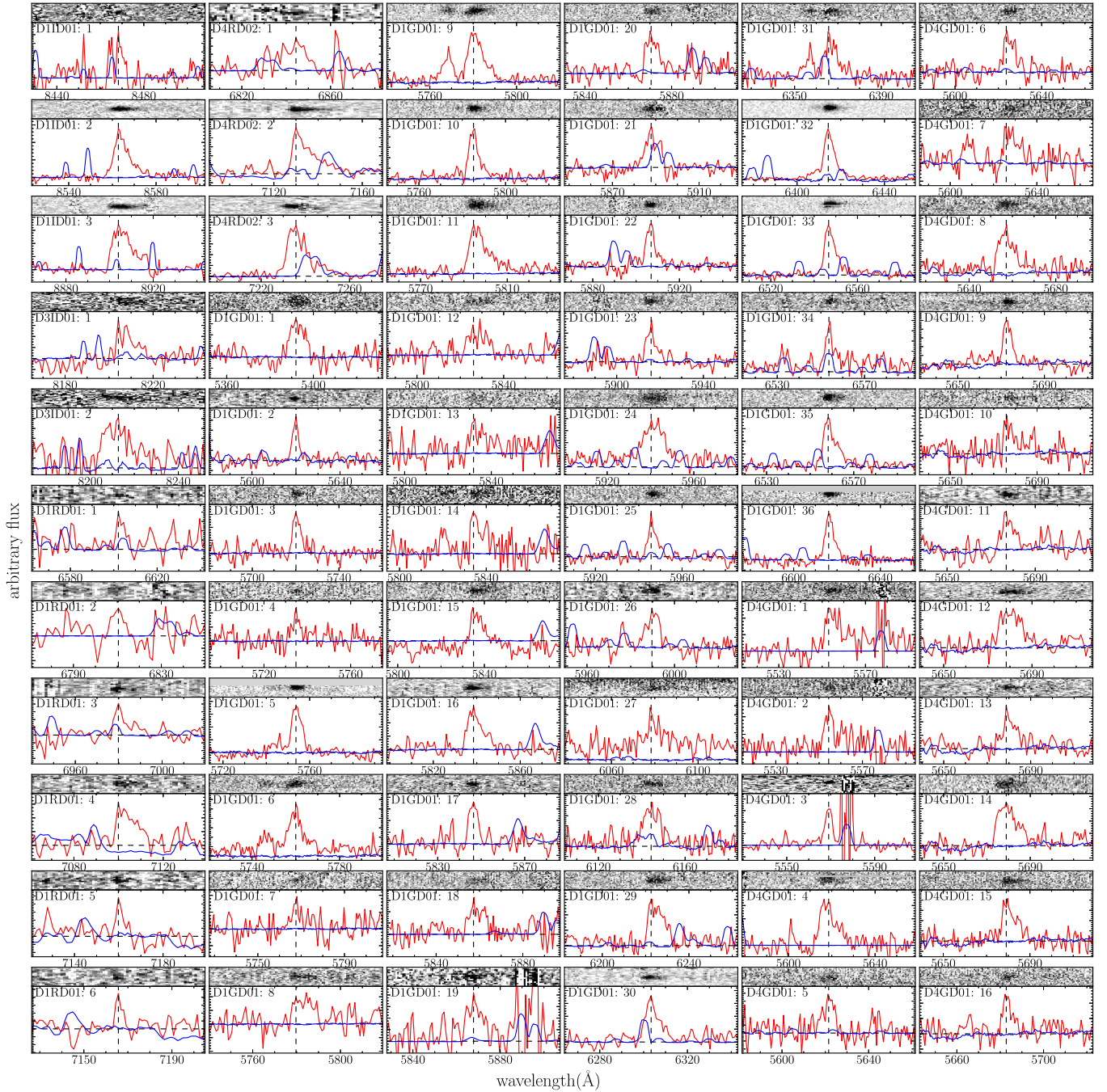


Figure 9. Spectra of all dropout galaxies having Ly α emission lines. The field and object IDs are indicated at the upper left corner (column 1 of Table 4). The vertical and horizontal dashed lines show the wavelength of Ly α emission and the zero level of flux, respectively.

especially, the significance of fifth nearest is less than 0.01. In contrast, there are no significant differences in the distribution of sixth or higher nearest galaxies. These results suggest that the protocluster has a subgroup consisting of six galaxies; therefore, the subgroup cannot be seen in the distribution of the sixth or higher nearest galaxies, which are consistent with the random distribution. The six galaxies constituting the subgroup are defined by having a shorter separation than 1.0 physical Mpc from the fifth nearest galaxies (ID = 11–16). The distributions of first and second nearest galaxies could also be divided into two groups of shorter and longer separations, though they are not so significant ($p \sim 0.2$), due to focusing on too small a scale. These six galaxies are

indicated by red points in Figure 23 and are located near the center of the protocluster. There are several galaxies in the region surrounding the core, which could assemble into the core to form a rich cluster. This is in clear contrast to what we saw in the protocluster at $z \sim 6$, which was found to have several small subgroups, like galaxy pairs (Toshikawa et al. 2014). Although we have only one protocluster at each redshift, if they are the progenitor and descendant of each other, the transformation of protocluster internal structure from $z \sim 6$ to $z \sim 4$ may be indicative of the virializing process over cosmic time, whereby protoclusters dynamically evolve into a more and more concentrated structure. At $z \sim 2-3$, the virializing process would not be completed yet, though there

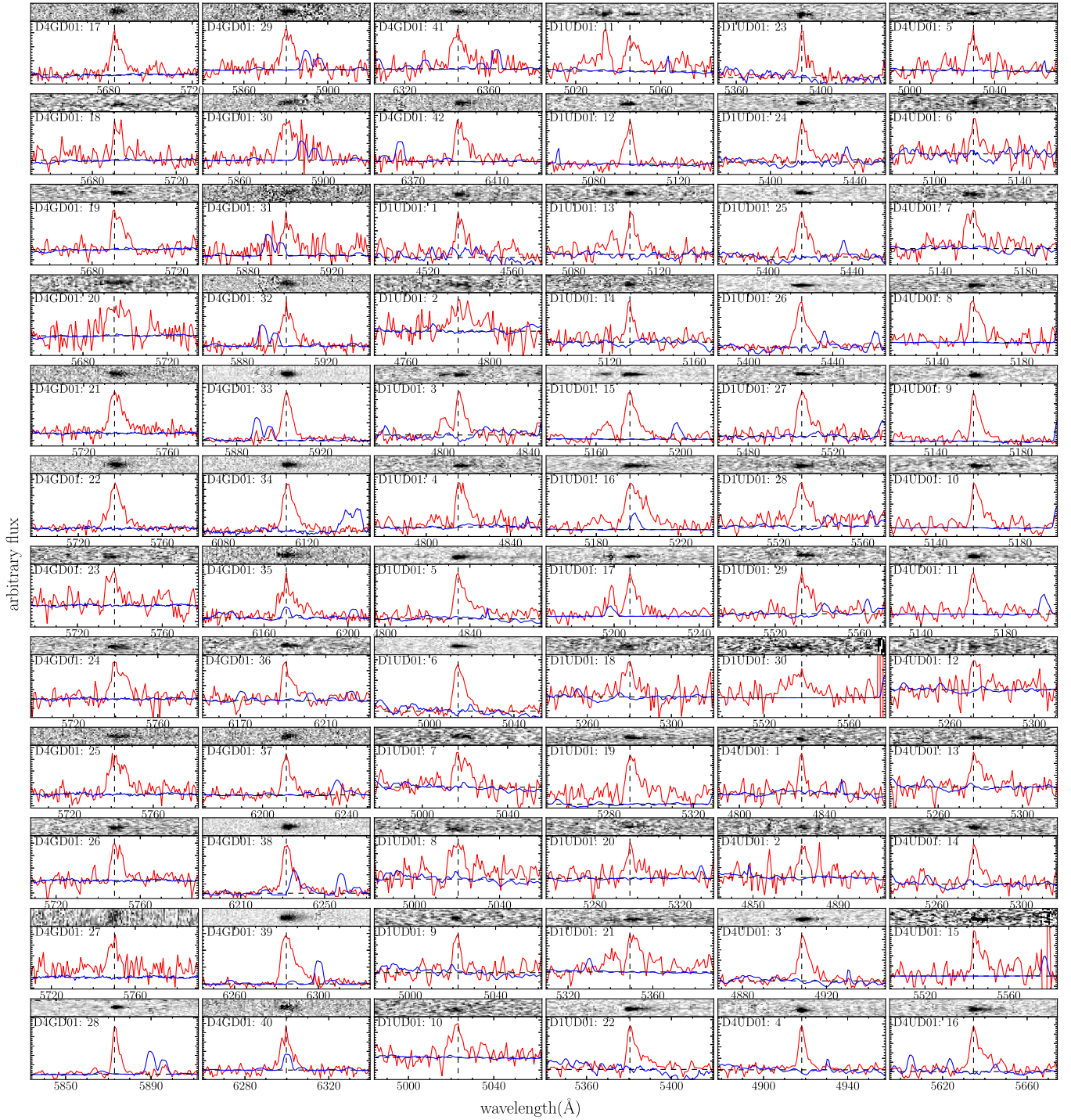


Figure 9. (Continued.)

are richer protoclusters where some massive and passive galaxies have already appeared. The internal structures of some protoclusters have been more closely investigated using extensive spectroscopy, and some protoclusters were found to have significant substructure (Kuiper et al. 2011, 2012). Therefore, even at the same redshift, protoclusters could have a large variety of internal structures. In this study based on a small number of protoclusters, the difference of internal structure found in the $z \sim 6$ and $z \sim 4$ protoclusters is assumed to result from the evolutionary phase of the representative

protoclusters. However, larger samples at each redshift will be required to statistically match progenitors and descendants, allowing us to study cluster formation over cosmic time (e.g., Chiang et al. 2013).

5.2. Rest-frame UV Properties of the Protocluster Members

We compared several galaxy properties between protocluster members and coeval field galaxies to investigate whether there are any differences that are due to their environment. The

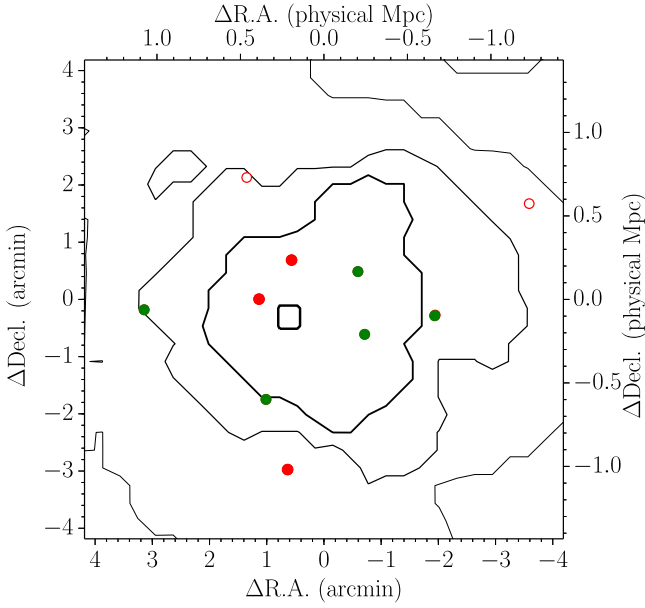


Figure 10. Sky distribution of *i*-dropout galaxies and number density contours in the D1ID01 region. Spectroscopically observed galaxies are marked by filled circles (red: $\text{Ly}\alpha$ -detected galaxies, green: $\text{Ly}\alpha$ -undetected galaxies), and spectroscopically unobserved galaxies are shown by open circles. The origin (0, 0) is (R.A., decl.) = (02:27:16.5, -04:50:49.6), which is defined as the center of the figure. The lines show the number density contours of *i*-dropout galaxies from 6σ to 0σ with a step of 2σ .

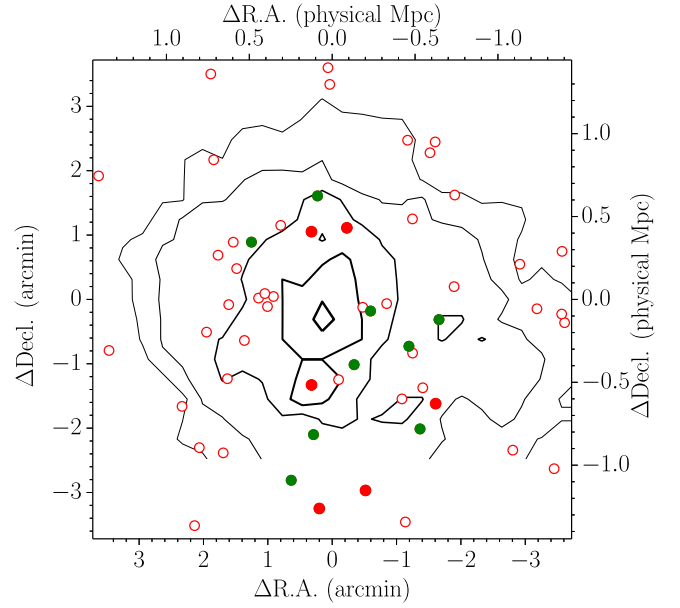


Figure 12. Sky distribution of *r*-dropout galaxies and number density contours in the D1RD01 region. Spectroscopically observed galaxies are marked by filled circles (red: $\text{Ly}\alpha$ -detected galaxies, green: $\text{Ly}\alpha$ -undetected galaxies), and spectroscopically unobserved galaxies are shown by open circles. The origin (0, 0) is (R.A., decl.) = (02:24:44.7, -04:55:37.9), which is defined as the center of the figure. The lines show the number density contours of *i*-dropout galaxies from 4σ to 0σ with a step of 1σ .

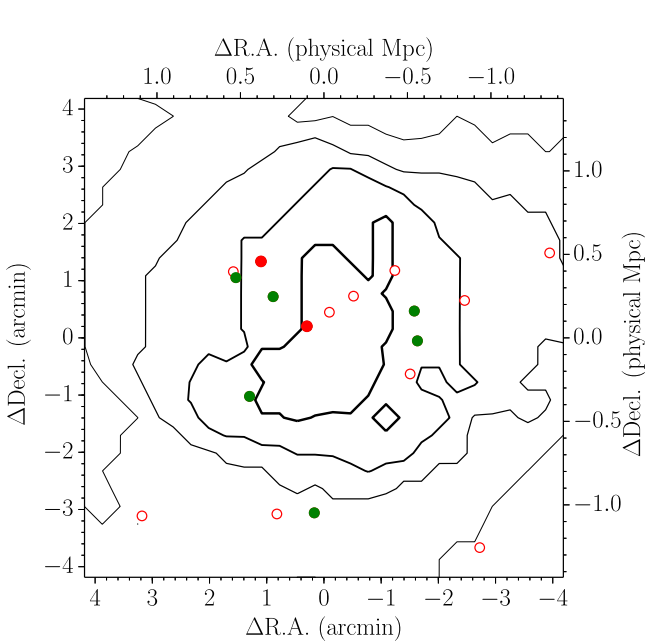


Figure 11. Sky distribution of *i*-dropout galaxies and number density contours in the D3ID01 region. Spectroscopically observed galaxies are marked by filled circles (red: $\text{Ly}\alpha$ -detected galaxies, green: $\text{Ly}\alpha$ -undetected galaxies), and spectroscopically unobserved galaxies are shown by open circles. The origin (0, 0) is (R.A., decl.) = (14:19:15.2, +52:56:02.2), which is defined as the center of the figure. The lines show the number density contours of *i*-dropout galaxies from 6σ to 0σ with a step of 2σ .

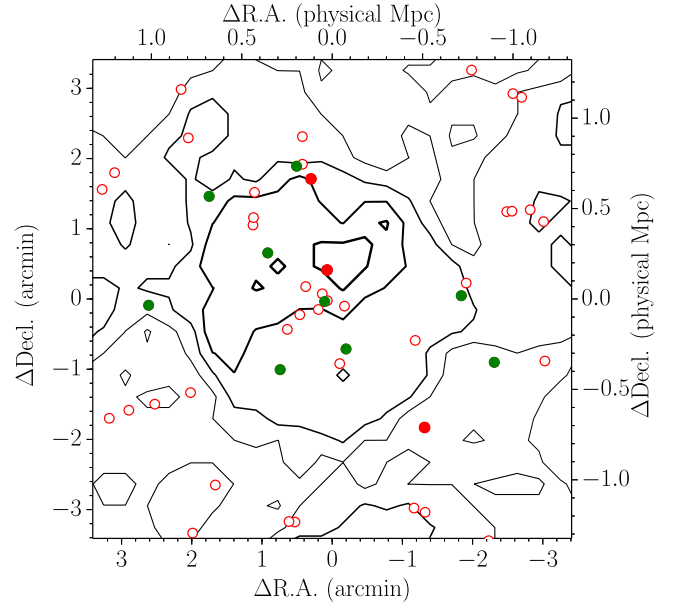


Figure 13. Sky distribution of *r*-dropout galaxies and number density contours in the D4RD02 region. Spectroscopically observed galaxies are marked by filled circles (red: $\text{Ly}\alpha$ -detected galaxies, green: $\text{Ly}\alpha$ -undetected galaxies), and spectroscopically unobserved galaxies are shown by open circles. The origin (0, 0) is (R.A., decl.) = (22:16:45.5, -17:29:44.7), which is defined as the center of the figure. The lines show the number density contours of *i*-dropout galaxies from 4σ to 0σ with a step of 1σ .

D4GD01 protocluster consists of 11 members, while the number of field *g*-dropout galaxies available is 67 by combining the galaxies in the D1 and D4 fields. The protocluster and field galaxies were identified by the same imaging and spectroscopic observations; thus, some sample

bias, if any, would affect both samples in the same way. This should allow us to make a fair comparison between protocluster and field galaxies. The average of $L_{\text{Ly}\alpha}$, M_{UV} , and EW_0 are described in Table 6. Since the D4GD01 protocluster has a core-like substructure, as mentioned in Section 5.1, the 11 members were divided into two groups of six galaxies in the

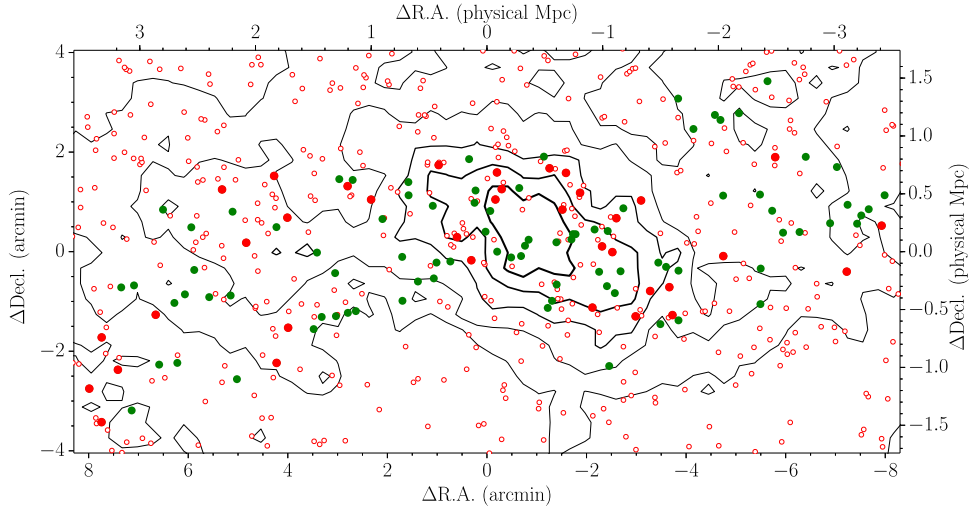


Figure 14. Sky distribution of g -dropout galaxies and number density contours in and around the D1GD01 region. Spectroscopically observed galaxies are marked by filled circles (red: $\text{Ly}\alpha$ -detected galaxies, green: $\text{Ly}\alpha$ -undetected galaxies), and spectroscopically unobserved galaxies are shown by open circles. The origin (0, 0) is (R.A., decl.) = (02:25:40.5, $-04:15:56.3$), which is defined as the center of the figure. The lines show the number density contours of i -dropout galaxies from 4σ to 0σ with a step of 1σ .

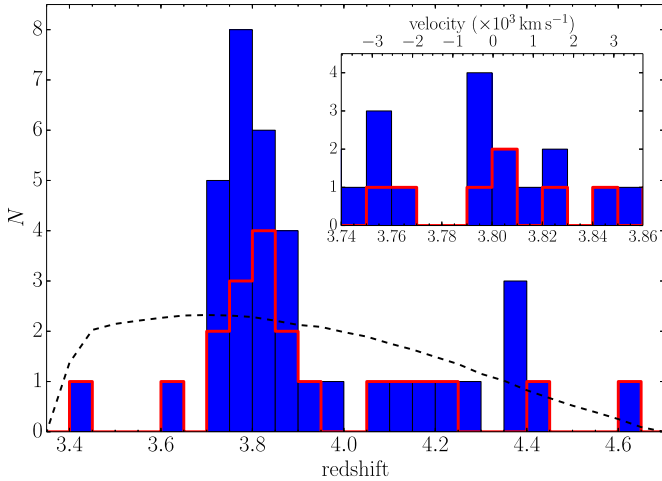


Figure 15. Redshift distribution of 36 g -dropout galaxies with the bin size of $\Delta z = 0.05$ in and around the D1GD01 region. The blue histogram shows all 36 galaxies, and the red line shows galaxies only in the D1GD01 region. The inset is a close-up of the protocluster redshift range, with a bin size of $\Delta z = 0.01$.

core and five galaxies in the outskirts. Table 6 also shows the average properties of these two subgroups. In Figure 25, the properties of individual protocluster and field galaxies are plotted on the M_{UV} and EW_0 diagram. We found that protocluster galaxies have significantly smaller EW_0 or $L_{\text{Ly}\alpha}$ luminosity than field galaxies (KS p -value is < 0.05); especially, fainter protocluster members in M_{UV} are strongly suppressed in their $\text{Ly}\alpha$ emissions compared with field galaxies. No significant difference between the core and the outskirts in the EW_0 and M_{UV} distribution was found.

Previous studies have found little evidence for significant differences between the properties of galaxies inside and outside protoclusters, at least at $z \gtrsim 4$ (Overzier et al. 2008, 2009b; Toshikawa et al. 2014). It is therefore interesting that we are finding a difference in the EW_0 or $L_{\text{Ly}\alpha}$ distributions between field and protocluster in the D4GD01 system at $z = 3.67$. This is perhaps an indication that the situation is changing around $z \sim 4$. One simple mechanism that could reduce the $\text{Ly}\alpha$ EW_0 would be dust, which traps $\text{Ly}\alpha$ photons.

If dust is a major reason for the small EW_0 , M_{UV} is expected to be systematically smaller in the protocluster because UV flux can also be easily attenuated by dust, as in the case with $\text{Ly}\alpha$ emission. However, we did not find any systematic difference in M_{UV} between the protocluster and field galaxies (see Table 6). Although dust attenuation does not seem to be the reason for this result, it is still possible that the amount of UV flux attenuated by dust is being compensated for by higher SFR or other effects related to UV emission; in that case, we would not find any difference in the distribution of apparent M_{UV} between protocluster and field galaxies even if there were a clear difference of dust attenuation. Therefore, in order to more directly estimate the dust attenuation, we compared the UV slope between protocluster and field galaxies. The UV slope of each g -dropout galaxy was determined from the $i - z$ color. However, since the i' -band image was significantly deeper (~ 1 mag) than the z' -band image, some g -dropout galaxies were not detected in the z' band. For the estimate of the UV slope, we therefore only used g -dropout galaxies that were detected in the z' -band image with $> 2\sigma$ significance (< 26.70 mag). Although this discordant depth between the i' - and z' -band images will lead to a bias in the estimate of UV slope, the protocluster and field galaxies would be equally biased because they were selected by the same criteria and from the same data set. The number of g -dropout galaxies used in the estimate was nine for the protocluster and 50 for the field. Note that there is no difference in the fraction of galaxies detected in the z' band between protocluster (9/11) and field (50/67). The UV slope was calculated from

$$\beta = -0.4 \times \frac{m_i - m_z}{\log_{10} \lambda_{\text{eff},i} - \log_{10} \lambda_{\text{eff},z}} - 2.0, \quad (1)$$

where λ_{eff} is the effective wavelength. The average β of the protocluster galaxies was $\beta = -1.88 \pm 0.38$, and that of the field galaxies was $\beta = -1.92 \pm 0.17$; thus, it would be hard to explain the difference in EW_0 simply by dust attenuation. It should be noted that the radiative process of $\text{Ly}\alpha$ photons to escape from a galaxy is very complicated and affected by many

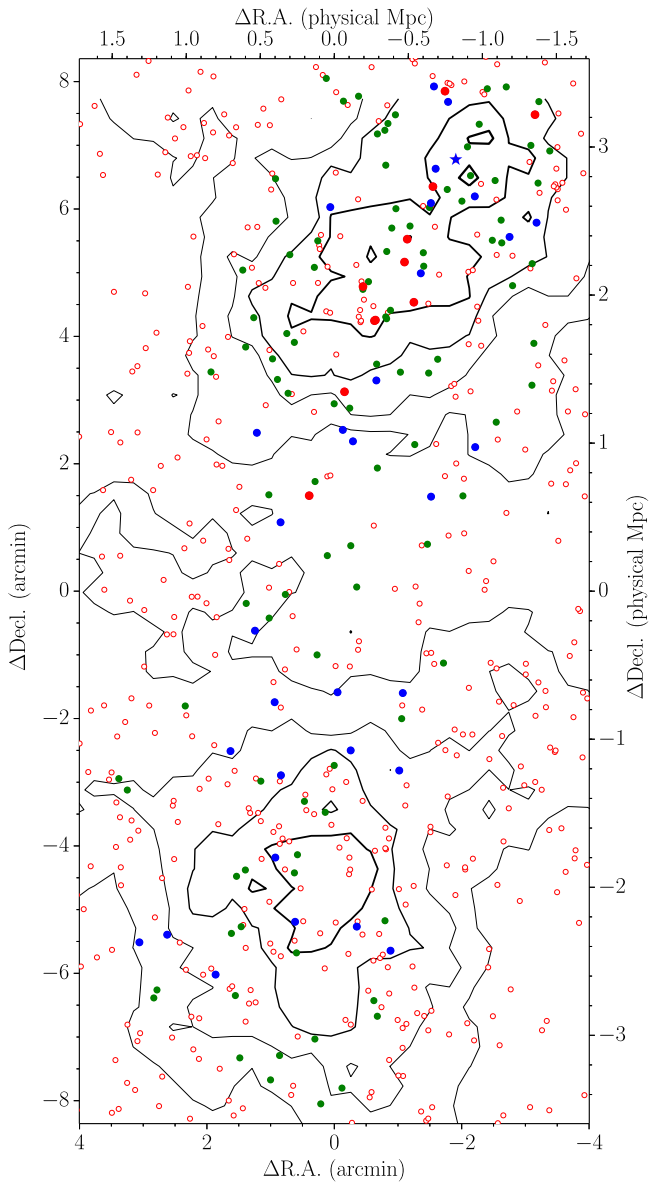


Figure 16. Sky distribution of g -dropout galaxies and number density contours in and around the D4GD01 region. Spectroscopically observed galaxies are marked by filled circles (red: protocluster members, blue: nonmembers, green: $\text{Ly}\alpha$ -undetected galaxies), and spectroscopically unobserved galaxies are shown by open circles. The blue star indicates the position of the AGN. The origin (0, 0) is (R.A., decl.) = (22:16:56.3, -17:23:21.9), which is defined as the center of the figure. The lines show the number density contours of i -dropout galaxies from 4σ to 0σ with a step of 1σ .

other quantities, such as dust geometry, gas kinematics, and outflow (e.g., Verhamme et al. 2008; Duval et al. 2014).

Neutral hydrogen gas within a protocluster is another possible reason for the small EW_0 . Cucciati et al. (2014) found a large amount of neutral hydrogen gas ($\sim 10^{12}$ – $10^{13} M_\odot$) in the intracluster space of a protocluster by examining spectra of background galaxies of a protocluster at $z = 2.9$, which showed absorption at the same wavelength as the observed $\text{Ly}\alpha$ of the protocluster. If the same is true in the D4GD01 protocluster, though our follow-up spectroscopy is not deep enough to check this even by stacking, a small EW_0 could be explained as being a result of resonant scattering by the intracluster neutral

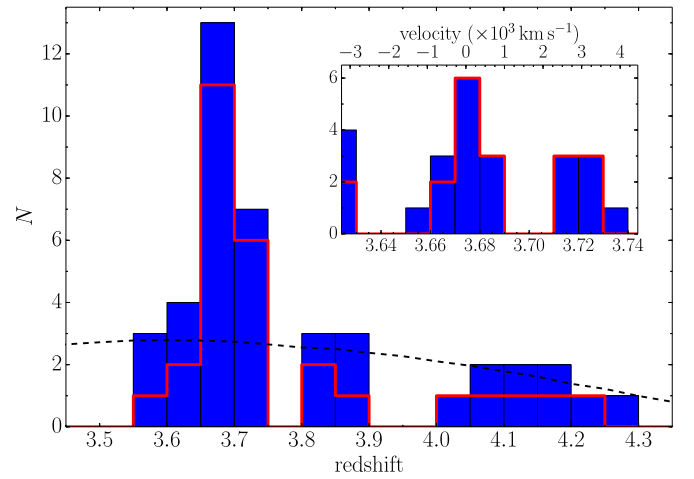


Figure 17. Redshift distribution of 42 g -dropout galaxies with the bin size of $\Delta z = 0.05$ in and around the D4GD01 region. The blue histogram shows all 42 galaxies, and the red line shows galaxies only in the D4GD01 region. The inset is a close-up of the protocluster redshift range, with a bin size of $\Delta z = 0.01$.

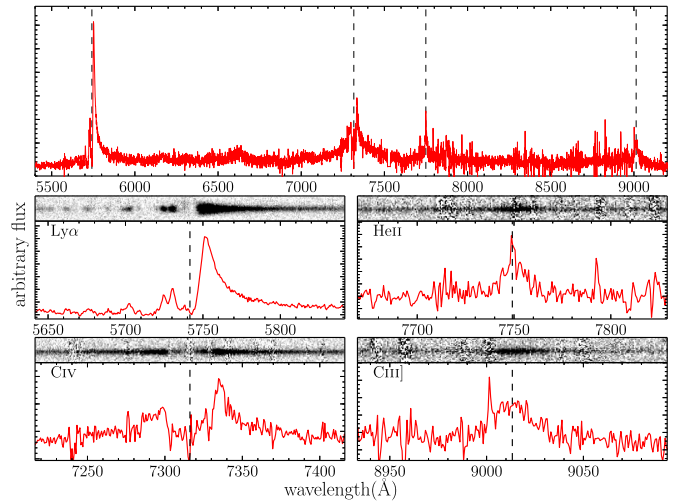


Figure 18. Spectra of the AGN in the D4GD01. The upper panel shows the full wavelength coverage of the AGN, and the four lower panels show emission lines that were clearly detected. The redshift was estimated by the peak wavelength of He II and C III , and the vertical dashed lines in the He II and C III panels indicate the peak of the emission line. The vertical dashed lines in the $\text{Ly}\alpha$ and C IV panels indicate the expected wavelength according to the redshift.

hydrogen gas. While the UV photons can penetrate neutral hydrogen gas, $\text{Ly}\alpha$ emission is scattered and diffused, consistent with our results. Suppose that a nearly mature protocluster, such as the D4GD01 protocluster, had already accumulated significant cold intracluster gas at $z = 3.67$; the intracluster gas would come either from the outside of the protocluster drawn in by the strong gravitational potential of the protocluster or could be brought in with the evolved member galaxies themselves through inflows and outflows.

Although it is difficult to identify the cause, we have found that the average EW_0 of $z = 3.67$ protocluster members is significantly smaller than that of field galaxies. However, it is still under debate how $\text{Ly}\alpha$ EW_0 depends on environments. Actually, in contrast with our study, Yamada et al. (2012) have

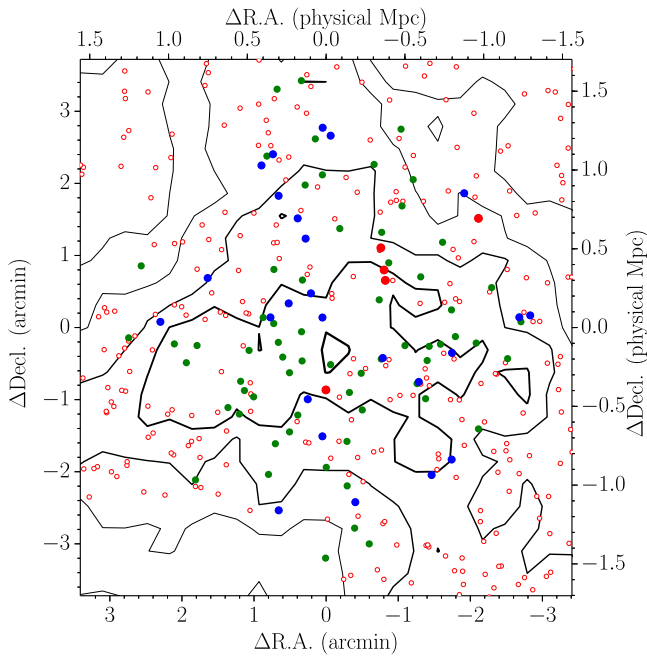


Figure 19. Sky distribution of u -dropout galaxies and number density contours in the D1UD01 region. Spectroscopically observed galaxies are marked by filled circles (red: protocluster members, blue: non-members, green: $\text{Ly}\alpha$ -undetected galaxies), and spectroscopically unobserved galaxies are shown by open circles. The origin (0, 0) is (R.A., decl.) = (02:24:35.4, -04:19:40.3), which is defined as the center of the figure. The lines show the number density contours of i -dropout galaxies from 4σ to 0σ with a step of 1σ .

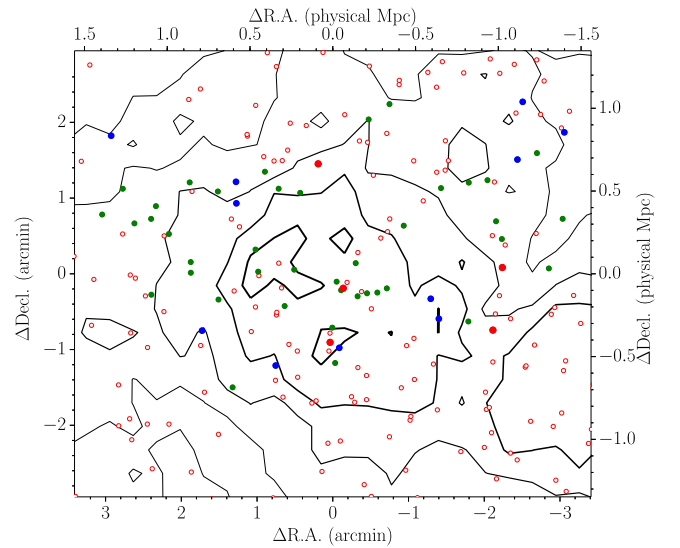


Figure 21. Sky distribution of u -dropout galaxies and number density contours in the D4UD01 region. Spectroscopically observed galaxies are marked by filled circles (red: protocluster members, blue: nonmembers, green: $\text{Ly}\alpha$ -undetected galaxies), and spectroscopically unobserved galaxies are shown by open circles. The origin (0, 0) is (R.A., decl.) = (22:14:04.0, -17:59:11.3), which is defined as the center of the figure. The lines show the number density contours of i -dropout galaxies from 4σ to 0σ with a step of 1σ .

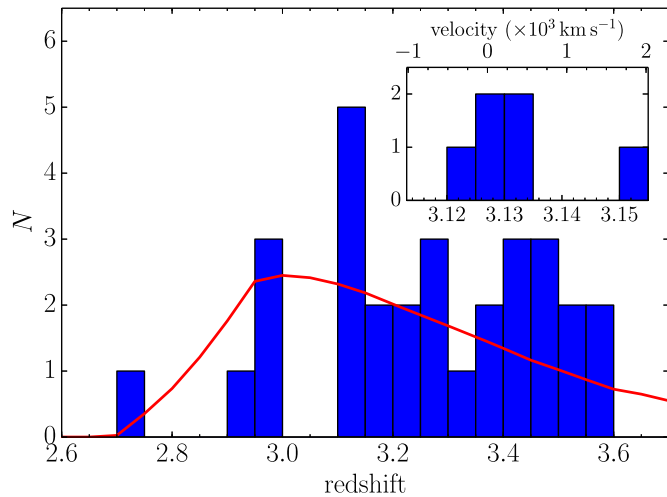


Figure 20. Redshift distribution of 30 u -dropout galaxies with the bin size of $\Delta z = 0.05$ in the D1UD01 region. The inset is a close-up of the protocluster redshift range, with a bin size of $\Delta z = 0.005$.

found larger EW_0 in the SSA22 protocluster at $z = 3.09$. Kuiper et al. (2012) reported a protocluster being composed of two subgroups at $z = 3.13$, where the one subgroup has larger EW_0 , but the other has smaller. Furthermore, there are some protoclusters that have no significant difference of $\text{Ly}\alpha$ EW_0 from that of field galaxies (Mawatari et al. 2012). Since the number of known protoclusters is limited even around $z \sim 3$ so far, a large-enough sample will be required to address a general

feature. This may have consequences for the measurement of the $\text{Ly}\alpha$ fraction (Ono et al. 2012; Treu et al. 2013), which is one of the ways to probe reionization at high redshifts. A detailed study of galaxy properties will be made in the future by combining multiwavelength data.

6. CONCLUSIONS

In this study, we have presented a protocluster survey from $z \sim 3$ to $z \sim 6$ in the CFHTLS Deep Fields. This survey was performed using wide-field imaging without using the preselection of common protocluster probes such as RGs and QSOs. Protocluster candidates were identified by measuring the surface number density of dropout galaxies, and the follow-up spectroscopic observations identified three real protoclusters. The major results and implications of this study are summarized below.

1. We investigated the sky distribution of u -, g -, r -, and i -dropout galaxies in the wide-field imaging of the CFHTLS Deep Fields and quantified the local surface number density by counting galaxies within a fixed aperture. We selected a total of 21 overdense regions with an overdensity significance greater than 4σ as protocluster candidates. The number density of protocluster candidates was approximately one candidate per 1 deg^2 area for each redshift sample based on a 4 deg^2 survey.
2. We investigated the relation between the overdensity at high redshifts and the descendent halo mass using light-cone models constructed from cosmological simulations. We selected galaxy samples with the same redshift distribution as the observations, and the same overdensity measuring procedure was applied to this simulated sample of dropout galaxies. A strong correlation between the overdensity at high redshifts and the descendent halo

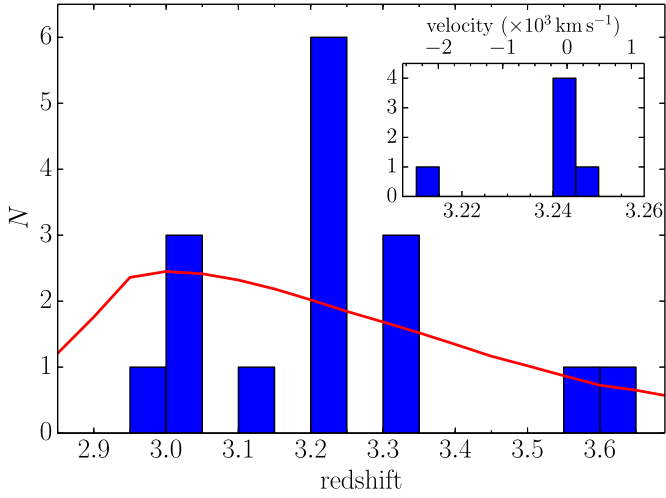


Figure 22. Redshift distribution of 16 u -dropout galaxies with the bin size of $\Delta z = 0.05$ in the D4UD01 region. The inset is a close-up of the protocluster redshift range, with a bin size of $\Delta z = 0.005$.

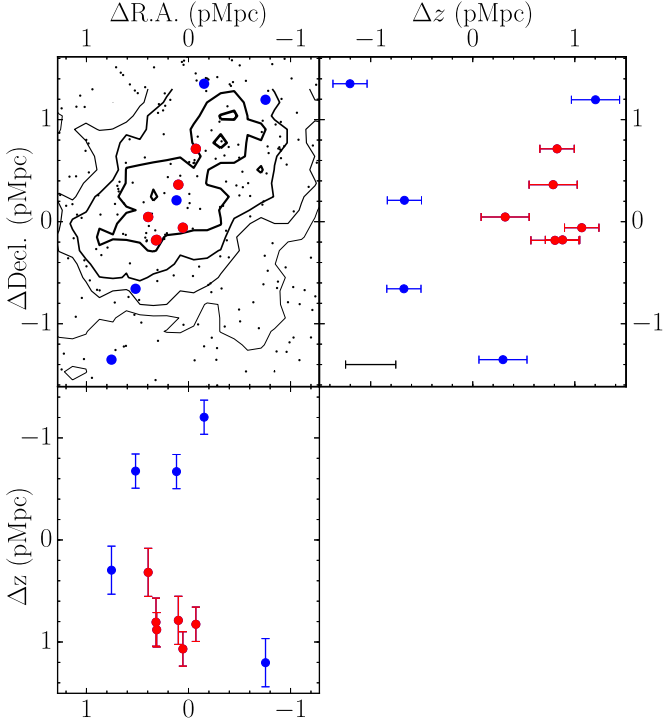


Figure 23. Three-dimensional distribution of the protocluster galaxies in the D4GD01 region. The filled circles represent the 11 protocluster galaxies (six red ones are galaxies residing in the core region, and five blue in the outskirts region), and the dots are g -dropout galaxies. Note that the origin (0, 0) of this figure is defined as (R.A., decl.) = (22:16:50.4, -17:18:41.6). The black scale bar shown in the lower left corner of the top right panel represents the typical difference expected between the apparent (i.e., including the effect of peculiar velocities) and geometrical redshifts.

mass at $z = 0$ was found, and $\gtrsim 76\%$ of the overdense regions with significance over 4σ are expected to grow into dark matter halos with $M > 10^{14} M_{\odot}$ at $z = 0$. Despite significant projection effects, the model predicts that protoclusters can be identified with high confidence by measuring the surface overdensity significance. In addition, the model predicts that protocluster members

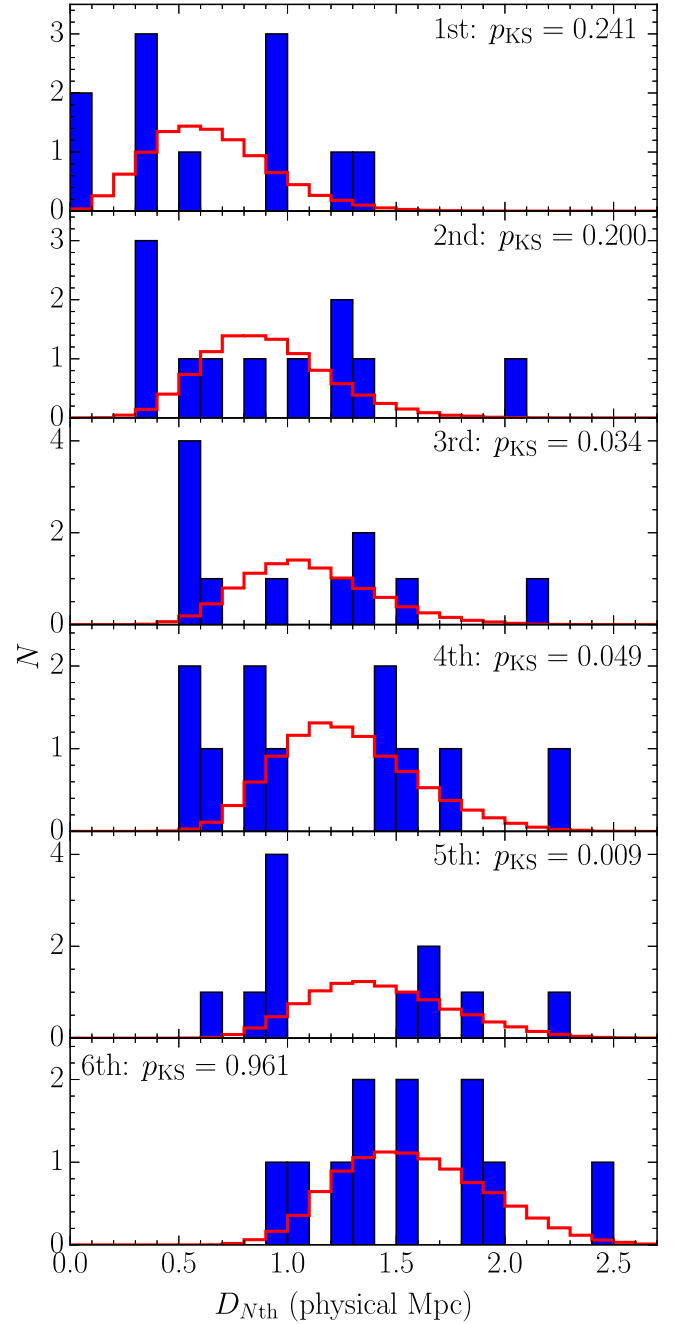


Figure 24. Distribution of the separation from the first (top) to sixth (bottom) nearest galaxy in the D4GD01 protocluster (blue histogram). The red line shows an expected distribution assuming that 11 galaxies are randomly distributed in the same volume of the D4GD01 protocluster.

are, on average, spread within a sphere of 2 physical Mpc radius.

3. We carried out follow-up spectroscopic observations of eight protocluster candidates between $z \sim 3$ and $z \sim 6$ to confirm whether these were genuine protoclusters. The redshifts of all the protocluster members were determined by detecting their Ly α emission lines, and no apparent contamination from low-redshift interlopers was found in our spectroscopic observation. Although the completeness of slit allocation to dropout galaxies in a protocluster candidate is about 30%–60%, three of the eight

Table 6Average of Observed Properties of g -Dropout Galaxies in the CFHTLS Deep Fields

	$L_{\text{Ly}\alpha}$ (10^{42} erg s $^{-1}$)	M_{UV} (mag)	EW_0 (Å)
protocluster	1.46 ± 0.76	-19.47 ± 0.51	24.48 ± 12.20
field	2.34 ± 1.67	-19.45 ± 0.74	41.68 ± 39.00
p -value ^a	0.04	0.67	0.03
core	1.69 ± 0.75	-19.84 ± 0.60	22.45 ± 10.03
outskirt	1.20 ± 0.68	-19.29 ± 0.26	27.13 ± 14.60

Note.

^a Using the KS test, the distributions of observed properties are compared between protocluster and field galaxies.

protocluster candidates were confirmed to be genuine protoclusters by ascertaining that their member galaxies were clustering in both the spatial and redshift directions (<2 physical Mpc) with $\sim 3\sigma$ significance with more than five members spectroscopically identified. Spectroscopy revealed that chance alignment of dropout galaxies mimics an overdensity region for one candidate. There are some signatures of clustering of several galaxies in the other four protocluster candidates at $z \sim 5$ –6; however, the numbers of spectroscopically confirmed galaxies are still too small to conclude that they are genuine protoclusters. Although there are still many protocluster candidates to follow up spectroscopically, our method to search for protoclusters utilizing wide-field imaging is reliable and sufficiently effective to construct high-redshift protocluster samples based on the success rate of follow-up observations.

- We investigated the internal structure of the D4GD01 protocluster at $z = 3.67$ based on its 11 spectroscopically confirmed members. The distribution of member galaxies exhibits a core-like structure: half of the members are concentrated in a small central region (<0.5 physical Mpc), and the others in the outskirts (~ 1.0 physical Mpc). The result implies that this protocluster might be on the way to evolving into a virialized structure, though further protocluster samples are required to confirm a general trend.
- The D4GD01 protocluster galaxies have significantly smaller EW_0 than coeval field galaxies, while there is no difference in M_{UV} . We considered two physical mechanisms that may lead to this difference: the first is dust in protocluster galaxies, and the second is intracluster neutral hydrogen gas. Although we were not able to draw definite conclusions based on current data, the UV slope was found not to favor an interpretation whereby the difference in EW_0 is attributed only to dust. Our finding of a smaller EW_0 implies that the properties of protocluster galaxies might be affected by the environment already at $z = 3.67$.

Although we were successful in finding at least three new protoclusters using wide-field imaging and spectroscopy in a blank deep field, the sample size is still too small to elucidate a general picture of the structure formation and the evolution of environmental effects. However, this study is an important benchmark for finding large numbers of protoclusters and tracing the cluster-formation history in upcoming deep, wide

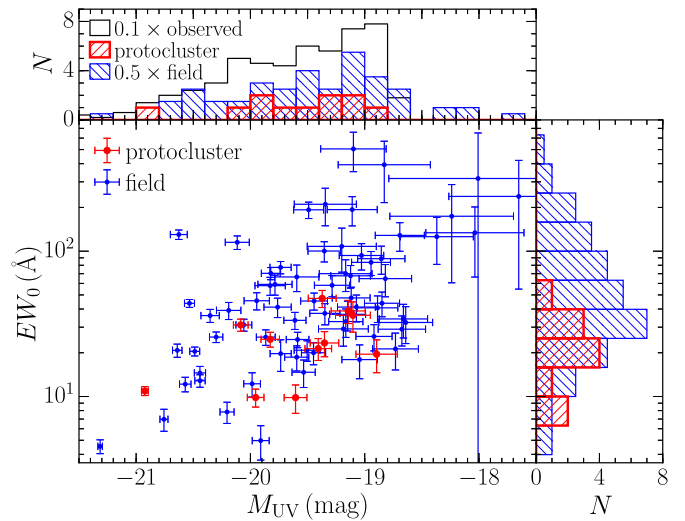


Figure 25. EW_0 versus M_{UV} of spectroscopically confirmed g -dropout galaxies in the CFHTLS D1 and D4. The histograms in the top and right panels show the EW_0 and M_{UV} distributions of the protocluster and field galaxies. Red and blue colors represent the protocluster and field galaxies in all three panels, respectively. In the histogram of M_{UV} (top), spectroscopically observed g -dropout galaxies are also shown by the black line, which is useful for evaluating the magnitude distribution of the targets and the $\text{Ly}\alpha$ detection rate in our follow-up spectroscopy. For clarity, the histograms of observed and field galaxies were multiplied by a factor of 0.1 and 0.5, respectively. The M_{UV} of observed galaxies (black), including $\text{Ly}\alpha$ -undetected galaxies, are estimated from the i' -band magnitude, which is free from IGM absorption and $\text{Ly}\alpha$ emission at $z \sim 3.8$, by assuming a flat UV slope; on the other hand, the M_{UV} of $\text{Ly}\alpha$ -detected galaxies (red and blue) are calculated based on a combination of the broadband photometry and the $\text{Ly}\alpha$ flux, as described in Section 4.3.

surveys using identical techniques. Using the new instrument Hyper SuprimeCam (HSC) on the Subaru telescope, we are performing an unprecedented wide and deep survey over the next four years. The HSC strategic survey consists of three layers: the WIDE layer covers 1400 deg^2 with the i -band depth of $m_i = 26.0$, the Deep layer 28 deg^2 with $m_i = 26.8$, and the Ultradeep layer 3.5 deg^2 with $m_i = 27.4$. From this study, we estimate that the number of protoclusters that the HSC survey will be able to find will be >20 at $z \sim 5$ –6 and >1000 at $z \sim 3$ –4. From 2018 onward, spectroscopic follow-up of tens of thousands of dropout galaxies selected from the HSC Deep layer will be performed using the large multiplexing capability of the Prime Focus Spectrograph, also on the Subaru telescope. This will allow us to understand the cluster-formation process all the way from reionization to the present day.

The CFHTLS data used in this study are based on observations obtained with MegaPrime/MegaCam, a joint project of CFHT and CEA/IRFU, at the Canada–France–Hawaii Telescope (CFHT), which is operated by the National Research Council (NRC) of Canada, the Institut National des Science de l’Univers of the Centre National de la Recherche Scientifique (CNRS) of France, and the University of Hawaii. This study is based in part on data products produced at Terapix available at the Canadian Astronomy Data Centre as part of the Canada–France–Hawaii Telescope Legacy Survey, a collaborative project of NRC and CNRS. This study is based on data collected at the Subaru, the W.M. Keck, and the Gemini North telescopes. The Subaru telescope is operated by the National Astronomical Observatory of Japan. The W.M. Keck telescope is operated as a scientific partnership among the

California Institute of Technology, the University of California, and the National Aeronautics and Space Administration. The W.M. Keck Observatory was made possible by the generous financial support of the W.M. Keck Foundation. The Gemini North telescope is operated by the Association of Universities for Research in Astronomy, Inc., under a cooperative agreement with the NSF on behalf of the Gemini partnership: the National Science Foundation (United States), the National Research Council (Canada), CONICYT (Chile), the Australian Research Council (Australia), Ministério da Ciência, Tecnologia e Inovação (Brazil) and Ministerio de Ciencia, Tecnología e Innovación Productiva (Argentina). We are grateful to the Subaru, W.M. Keck, and Gemini Observatory staff for their help with the observations, and we wish to recognize and acknowledge the very significant cultural role and reverence that the summit of Mauna Kea has always had within the indigenous Hawaiian community. The Millennium Simulation databases used in this study and the web application providing online access to them were constructed as part of the activities of the German Astrophysical Virtual Observatory (GAVO). We thank the anonymous referee for valuable comments and suggestions that improved the manuscript. This research was supported by the Japan Society for the Promotion of Science through Grants-in-Aid for Scientific Research 12J01607 and 15H03645.

REFERENCES

- Adams, S. M., Martini, P., Croxall, K. V., Overzier, R. A., & Silverman, J. D. 2015, *MNRAS*, **448**, 1335
- Aravena, M., Bertoldi, F., Carilli, C., et al. 2010, *ApJL*, **708**, L36
- Barkana, R., & Loeb, A. 1999, *ApJ*, **523**, 54
- Beers, T. C., Flynn, K., & Gebhardt, K. 1990, *AJ*, **100**, 32
- Bertin, E., & Arnouts, S. 1996, *A&AS*, **117**, 393
- Bouwens, R. J., Illingworth, G. D., Franx, M., & Ford, H. 2007, *ApJ*, **670**, 928
- Bouwens, R. J., Illingworth, G. D., Oesch, P. A., et al. 2012, *ApJ*, **754**, 83
- Bruzual, G., & Charlot, S. 2003, *MNRAS*, **344**, 1000
- Butcher, H., & Oemler, A., Jr. 1984, *ApJ*, **285**, 426
- Calzetti, D., Armus, L., Bohlin, R. C., et al. 2000, *ApJ*, **533**, 682
- Capak, P. L., Riechers, D., Scoville, N. Z., et al. 2011, *Natur*, **470**, 233
- Casey, C. M., Cooray, A., Capak, P., et al. 2015, *ApJL*, **808**, L33
- Chiang, Y.-K., Overzier, R., & Gebhardt, K. 2013, *ApJ*, **779**, 127
- Cucciati, O., Zamorani, G., Lemaux, B. C., et al. 2014, *A&A*, **570**, A16
- Curtis-Lake, E., McLure, R. J., Pearce, H. J., et al. 2012, *MNRAS*, **422**, 1425
- de Lapparent, V., Geller, M. J., & Huchra, J. P. 1986, *ApJL*, **302**, L1
- Digby-North, J. A., Nandra, K., Laird, E. S., et al. 2010, *MNRAS*, **407**, 846
- Dressler, A. 1980, *ApJ*, **236**, 351
- Duval, F., Schaerer, D., Östlin, G., & Laursen, P. 2014, *A&A*, **562**, A52
- Faber, S. M., Phillips, A. C., Kibrick, R. I., et al. 2003, *Proc SPIE*, **4841**, 1657
- Galametz, A., Stern, D., Pentericci, L., et al. 2013, *A&A*, **559**, A2
- Girardi, L., Groenewegen, M. A. T., Hatziminaoglou, E., & da Costa, L. 2005, *A&A*, **436**, 895
- Guo, Q., White, S., Boylan-Kolchin, M., et al. 2011, *MNRAS*, **413**, 101
- Gwyn, S. D. J. 2012, *AJ*, **143**, 38
- Hatch, N. A., Kurk, J. D., Pentericci, L., et al. 2011, *MNRAS*, **415**, 2993
- Hatch, N. A., Wylezalek, D., Kurk, J. D., et al. 2014, *MNRAS*, **445**, 280
- Henriques, B. M. B., White, S. D. M., Lemson, G., et al. 2012, *MNRAS*, **421**, 2904
- Hook, I. M., Jørgensen, I., Allington-Smith, J. R., et al. 2004, *PASP*, **116**, 425
- Hopkins, P. F. 2012, *MNRAS*, **420**, L8
- Inoue, A. K., Shimizu, I., Iwata, I., & Tanaka, M. 2014, *MNRAS*, **442**, 1805
- Ishigaki, M., Ouchi, M., & Harikane, Y. 2016, *ApJ*, **822**, 5
- Kacprzak, G. G., Yuan, T., Nanayakkara, T., et al. 2015, *ApJL*, **802**, L26
- Kashikawa, N., Aoki, K., Asai, R., et al. 2002, *PASJ*, **54**, 819
- Kashikawa, N., Kitayama, T., Doi, M., et al. 2007, *ApJ*, **663**, 765
- Kashikawa, N., Shimasaku, K., Malkan, M. A., et al. 2006, *ApJ*, **648**, 7
- Kodama, T., Tanaka, I., Kajisawa, M., et al. 2007, *MNRAS*, **377**, 1717
- Kubo, M., Uchimoto, Y. K., Yamada, T., et al. 2013, *ApJ*, **778**, 170
- Kuiper, E., Hatch, N. A., Miley, G. K., et al. 2011, *MNRAS*, **415**, 2245
- Kuiper, E., Hatch, N. A., Röttgering, H. J. A., et al. 2010, *MNRAS*, **405**, 969
- Kuiper, E., Venemans, B. P., Hatch, N. A., Miley, G. K., & Röttgering, H. J. A. 2012, *MNRAS*, **425**, 801
- Kulas, K. R., McLean, I. S., Shapley, A. E., et al. 2013, *ApJ*, **774**, 130
- Kurk, J. D., Pentericci, L., Röttgering, H. J. A., & Miley, G. K. 2004, *A&A*, **428**, 793
- Lehmer, B. D., Alexander, D. M., Geach, J. E., et al. 2009, *ApJ*, **691**, 687
- Lemaux, B. C., Cucciati, O., Tasca, L. A. M., et al. 2014, *A&A*, **572**, A41
- Madau, P. 1995, *ApJ*, **441**, 18
- Matsuda, Y., Yamada, T., Hayashino, T., et al. 2011, *MNRAS*, **410**, L13
- Mawatari, K., Yamada, T., Nakamura, Y., Hayashino, T., & Matsuda, Y. 2012, *ApJ*, **759**, 133
- Meiksin, A. 2006, *MNRAS*, **365**, 807
- Miley, G. K., Overzier, R. A., Tsvetanov, Z. I., et al. 2004, *Natur*, **427**, 47
- Miller, T. B., Hayward, C. C., Chapman, S. C., & Behroozi, P. S. 2015, *MNRAS*, **452**, 878
- Muldrew, S. I., Hatch, N. A., & Cooke, E. A. 2015, *MNRAS*, **452**, 2528
- Ono, Y., Ouchi, M., Mobasher, B., et al. 2012, *ApJ*, **744**, 83
- Ouchi, M., Shimasaku, K., Akiyama, M., et al. 2005, *ApJL*, **620**, L1
- Overzier, R., Lemson, G., Angulo, R. E., et al. 2013, *MNRAS*, **428**, 778
- Overzier, R. A., Bouwens, R. J., Cross, N. J. G., et al. 2008, *ApJ*, **673**, 143
- Overzier, R. A., Guo, Q., Kauffmann, G., et al. 2009a, *MNRAS*, **394**, 577
- Overzier, R. A., Shu, X., Zheng, W., et al. 2009b, *ApJ*, **704**, 548
- Popesso, P., Rodighiero, G., Saintonge, A., et al. 2011, *A&A*, **532**, A145
- Salpeter, E. E. 1955, *ApJ*, **121**, 161
- Schlafly, E. F., & Finkbeiner, D. P. 2011, *ApJ*, **737**, 103
- Shimakawa, R., Kodama, T., Tadaki, K.-i., et al. 2015, *MNRAS*, **448**, 666
- Smolcic, V., Miettinen, O., Tomicic, N., et al. 2016, arXiv:1604.01775
- Springel, V., White, S. D. M., Jenkins, A., et al. 2005, *Natur*, **435**, 629
- Stark, D. P., Ellis, R. S., Bunker, A., et al. 2009, *ApJ*, **697**, 1493
- Stark, D. P., Ellis, R. S., & Ouchi, M. 2011, *ApJL*, **728**, L2
- Steidel, C. C., Adelberger, K. L., Dickinson, M., et al. 1998, *ApJ*, **492**, 428
- Steidel, C. C., Adelberger, K. L., Shapley, A. E., et al. 2000, *ApJ*, **532**, 170
- Steidel, C. C., Adelberger, K. L., Shapley, A. E., et al. 2005, *ApJ*, **626**, 44
- Tamura, Y., Iono, D., Wilner, D. J., et al. 2010, *ApJ*, **724**, 1270
- Thomas, R., Le Fèvre, O., Cassata, V. L. B. P., et al. 2014, arXiv:1411.5692
- Toshikawa, J., Kashikawa, N., Ota, K., et al. 2012, *ApJ*, **750**, 137
- Toshikawa, J., Kashikawa, N., Overzier, R., et al. 2014, *ApJ*, **792**, 15
- Tran, K.-V. H., Papovich, C., Saintonge, A., et al. 2010, *ApJL*, **719**, L126
- Trenti, M., Bradley, L. D., Stiavelli, M., et al. 2012, *ApJ*, **746**, 55
- Treu, T., Schmidt, K. B., Trenti, M., Bradley, L. D., & Stiavelli, M. 2013, *ApJL*, **775**, L29
- Valentino, F., Daddi, E., Strazzullo, V., et al. 2015, *ApJ*, **801**, 132
- van der Burg, R. F. J., Hildebrandt, H., & Erben, T. 2010, *A&A*, **523**, A74
- Venemans, B. P., Röttgering, H. J. A., Miley, G. K., et al. 2007, *A&A*, **461**, 823
- Verhamme, A., Schaerer, D., Atek, H., & Tapken, C. 2008, *A&A*, **491**, 89
- Viswanathan, N., & Sandage, A. 1977, *ApJ*, **216**, 214
- Walter, F., Decarli, R., Carilli, C., et al. 2012, *Natur*, **486**, 233
- Wylezalek, D., Galametz, A., Stern, D., et al. 2013, *ApJ*, **769**, 79
- Yamada, T., Nakamura, Y., Matsuda, Y., et al. 2012, *AJ*, **143**, 79
- Zirm, A. W., Stanford, S. A., Postman, M., et al. 2008, *ApJ*, **680**, 224